②

ESC-TR-93-236

AD-A272 912

Technical Report
984

Downlink Acquisition and Tracking Procedures for the ASCAMP Satellite Communications Terminal

DTIC
ELECTE
NOV 15 1993
S E D

R.J. Figucia

14 September 1993

Lincoln Laboratory
MASSACHUSETTS INSTITUTE OF TECHNOLOGY
LEXINGTON, MASSACHUSETTS

Prepared for the Department of the Army under Air Force Contract F19628-90-C-0002.

Approved for public release; distribution is unlimited.

93-27784

This report is based on studies performed at Lincoln Laboratory, a center for research operated by Massachusetts Institute of Technology. The work was sponsored by the Department of the Army under Air Force Contract F19628-90-C-0002.

This report may be reproduced to satisfy needs of U.S. Government agencies.

The ESC Public Affairs Office has reviewed this report, and it is releasable to the National Technical Information Service, where it will be available to the general public, including foreign nationals.

This technical report has been reviewed and is approved for publication.

FOR THE COMMANDER

Gary Tutungian

Gary Tutungian
Administrative Contracting Officer
Directorate of Contracted Support Management

Non-Lincoln Recipients

PLEASE DO NOT RETURN

Permission is given to destroy this document when it is no longer needed.

MASSACHUSETTS INSTITUTE OF TECHNOLOGY
LINCOLN LABORATORY

DOWNLINK ACQUISITION AND TRACKING PROCEDURES FOR THE ASCAMP SATELLITE COMMUNICATIONS TERMINAL

R.J. FIGUCIA
Group 66

DTIC QUALITY INSPECTED 5

Accesion For		
NTIS CRA&I	☒	
DTIC TAB	☐	
Unannounced	☐	
Justification		
By		
Distribution /		
Availability Codes		
Dist	Avail and / or Special	
A-1		

TECHNICAL REPORT 984

14 SEPTEMBER 1993

Approved for public release; distribution is unlimited.

LEXINGTON MASSACHUSETTS

ABSTRACT

The advanced single-channel antijam man portable (ASCAMP) terminal was developed at MIT Lincoln Laboratory as a proof of concept for the Army's SCAMP terminal. ASCAMP is a 30-lb, extremely high frequency (EHF) satellite communications terminal that is capable of operating from 75 to 2,400 bps with low inclination, geosynchronous FLTSAT EHF package and Milstar satellites. The terminal was designed to be carried, set up, and operated by a single user. In many instances the control algorithms have been designed to compensate for simplifications made in the hardware to keep terminal size, weight, and power to a minimum. This report describes the procedures implemented in the ASCAMP terminal to locate the satellite and synchronize with its downlink. It contains descriptions of the timing and pointing requirements, the procedures for acquisition and tracking, and the measured performance.

ACKNOWLEDGMENTS

The author would like to acknowledge Pat Hirschler-Marchand for laying the groundwork for ASCAMP acquisition [1] and to all the ASCAMP development team members, especially Edward Acosta, George Gorski-Popiel, Marie Heath, Judith LaRocca, John Siemasko, and Chester Small, who were involved in the development of hardware and software needed to execute and test the acquisition procedures described.

TABLE OF CONTENTS

LIST OF ILLUSTRATIONS

LIST OF TABLES

1. INTRODUCTION AND BACKGROUND

1.1 TIMING ISSUES

The ASCAMP terminal reduces its battery requirements by using two system clocks: a low-power "standby" clock that keeps time while the terminal is powered down and a more precise, higher power working clock that is used only when the terminal is operational. In its normal mode the terminal initializes its working clock from the time on the standby clock, which is adjusted by a correction term that is stored from the previous operation. There is also a backup mode in which the working clock is initialized from a wrist watch.

1.1.1 Initial Timing Errors Affecting Acquisition

The standby clock uses a temperature-controlled crystal oscillator (TCXO) that is assumed to have a conservative worst-case accuracy of 2 parts in 10^{-6} at any time within a year of tuning. The uncertainty in setting the working clock corresponds to the possible clock drift since the last operation due to the TCXO accuracy. ASCAMP determines the time search window needed for acquisition according to the equation

$$\text{NORMAL MODE:} \quad T_{\text{SEARCH ACQ}} = \pm\, 2 \times 10^{-6} \times \text{DOWN TIME.} \tag{1}$$

For example, a terminal that has been off for one month begins acquisition with a time search window of ±5 s. If the oscillator is changed or the period between oscillator tunings is expected to be longer than one year, then the search window must be adjusted accordingly.

In the backup mode the working clock is initialized from a wrist watch with the user specifying the time uncertainty, T_U, up to a maximum of 60 s or accepting the default of ±5 s. In this mode the time search window is defined as

$$\text{BACKUP MODE:} \quad T_{\text{SEARCH ACQ}} = \pm\, T_U. \tag{2}$$

In either normal or backup mode the minimum time search is ±30 ms.

Errors in the predicted range delay add to the initial timing uncertainty; however, as long as the orbital parameters used for prediction are less than one month old, the range error will have an insignificant effect on the time uncertainty[1] for the large time search windows used. During coarse acquisition, timing drifts due to the working clock's frequency errors can also be neglected because the granularity of the time hypotheses is greater than the maximum drift expected for the acquisition period.

---

[1] With highly inclined satellites, the range has much higher rates of change and its influence on the search window becomes more of a concern.

1.1.2 Timing Errors Affecting Tracking

The working clock that is used from the start of acquisition until the terminal is powered down uses a tactical miniature crystal oscillator (TMXO). The TMXO is specified to have a frequency accuracy of ±3 parts in 10^{-8} at the end of one year without tuning. The resulting maximum clock drift of 30 ns/s must be corrected using a closed-loop time tracking procedure. Changes in the range due to expected satellite motion create time drifts that must also be corrected by the time tracking algorithm. The range rates for operation with low inclination geosynchronous satellites result in a typical worst-case clock drift of 60 ns/s. The ASCAMP time tracking system must compensate for a worst-case combined drift of 90 ns/s.

1.2 POINTING ISSUES

ASCAMP determines its initial pointing angles from ephemeris calculations using Kepler's equations and then transforms the calculated angles to antenna motor angles that account for the fact that the terminal's base may not be level. The terminal estimates the motor angles associated with a level antenna using an automatic leveling procedure. The magnetic heading of the antenna in its level position is then approximated based on a compass reading and is factored into the transformation. A terminal-centered coordinate system is defined with respect to the plane tangent to the earth at the terminal point. It is chosen as the pointing reference for acquisition, pull-in, and tracking so that the search windows may be specified with respect to tilt and cross-tilt, loosely referred to as "elevation" and "azimuth" in this report.

1.2.1 Components of Pointing Uncertainty

Table 1 lists the main factors that contribute to pointing uncertainty in the ASCAMP terminal and gives estimates of their magnitudes. The combination of uncertainties in azimuth and elevation are accommodated by defining a spatial uncertainty for acquisition given by

$$S_{\mathrm{SEARCH\ ACQ}} = \pm 10.5^\circ \ \mathrm{Az} \times \pm 2^\circ \ \mathrm{El}. \tag{3}$$

TABLE 1

Pointing Uncertainty

Source	Magnitude	
	Az	El
Orbit prediction	0.4°	0.2°
Gear play	0.1°	0.1°
Leveling algorithm and calibration	0.5°	1.0°
Heading and magnetic variation	9.5°	0.5°
Total	10.5°	1.8°

Orbit Prediction. Ephemeris calculations used to determine open-loop azimuth and elevation pointing angles may be erroneous due to the implementation of the orbital model, errors in the user-entered longitude and latitude, and the use of old orbital elements. A large part of the prediction error is corrected through the acquisition and spatial pull-in procedures; however, as satellite position changes, open-loop corrections may reintroduce small errors. These errors can be corrected only by using a closed-loop tracking procedure.

Gear Play. Due to backlash in its gears, the antenna cannot be pointed with complete certainty to the desired angle. Wind causes the antenna angle to fluctuate by an amount equal to the magnitude of the backlash (β). The ASCAMP antenna controller uses a pointing algorithm to reduce these worst-case backlash errors. The algorithm assumes that the antenna controller has an *a priori* estimate of the backlash for the azimuth and elevation gear trains. The procedure causes the antenna to overshoot the intended position by $\beta/2$ in azimuth and elevation. It then reverses direction and moves the antenna by $\beta/2$ back to the desired point. In most cases the reverse motion by $\beta/2$ will not cause any physical movement to the antenna dish, but will move the gears so that the backlash uncertainty is split evenly on both sides of the desired pointing angle. The gear play in ASCAMP due to backlash is on the order of 0.2° but will be slightly different for each antenna drive assembly. By using the described pointing algorithm, the uncertainty is reduced to 0.1° in each direction.

Leveling and Calibration. The accuracy of the coordinate transformation depends on errors in level sensing. The leveling procedure relies on stored calibration angles to guide the automatic motion so that errors in these angles affect the accuracy of the level transformation. The sensing device in ASCAMP consists of a single mercury bubble switch that is subject to vibrational bounce that may cause additional inaccuracy. The combination of nominal calibration and leveling errors results in pointing uncertainties of approximately 0.5° in azimuth and 1° in elevation.

Heading and Magnetic Variation. After the terminal has performed the level operation, a pocket compass is used to determine the heading, i.e., terminal alignment in the cross-tilt direction with respect to magnetic north. The magnetic deviation is entered from a magnetic declination chart. A 9.5° uncertainty is allotted to account for a combination of compass inaccuracies, magnetic anomalies, and user errors. Due to the coordinate rotation, the uncertainty in heading affects the elevation, and its influence increases with terminal base inclination.

Motor Precision. The antenna motors can only move in multiples of 0.05° in azimuth and elevation. This finite precision causes a pointing uncertainty of 0.025° along each axis, which is assumed to be negligible in comparison with the other uncertainties.

1.2.2 Overview of Pointing

The pointing angles used in ASCAMP are divided into two components that are tracked separately throughout operation: an open-loop pointing angle and a closed-loop correction. The open-loop pointing angle is updated every 20 s by making a new ephemeris calculation. It has azimuth and elevation components referred to as (a_t, e_t) in terminal-centered coordinates. The terminal uses closed-loop tracking to correct for the pointing uncertainties described. The closed-loop pointing corrections $(\Delta a, \Delta e)$ are defined in the terminal-centered coordinate system and are updated periodically. The final pointing angle in terminal-centered coordinates is determined by combining the open-loop and closed-loop components to give

$$\text{POINTING HYPOTHESIS:}\quad s_o = (a_t + \Delta a,\ e_t + \Delta e)\ . \tag{4}$$

Prior to initial coarse acquisition, the closed-loop corrections Δa and Δe are set to zero, and the pointing hypothesis is based solely on the ephemeris angles (a_t, e_t). Unlike the time offsets, which are remembered from the previous operation, the pointing offsets are not stored when the terminal is shut off. They are, however, remembered from one acquisition to the next during a single operating session. Each time a new pointing hypothesis is determined, it is transformed into antenna motor angles to be used by the antenna controller.

1.3 OVERVIEW OF ACQUISITION AND TRACKING

The acquisition, pull-in, and tracking procedures are designed to correct for typical timing and pointing errors associated with terminal operation. The acquisition and pull-in procedures reduce timing uncertainty from a maximum of 60 s down to 50 ns to allow operation in the least robust communication mode with a 0.2-dB timing loss. They also reduce the pointing uncertainty from 10.5° in azimuth and 2° in elevation to a total of 0.25°, for maximum pointing losses of 0.4 dB on the downlink and 1.6 dB on the uplink. The acquisition procedure is designed to have a probability of false acquisition of 10^{-5} and a probability of missed detection of 10^{-3}. The time tracking procedure results in a timing accuracy of 50 ns for clock drifts up to 100 ns/s. The spatial tracking procedure sustains a 0.25° accuracy for a typical geosynchronous orbit and is capable of tracking angle changes of 0.01°/min.

Figure 1 shows the sequence of acquisition and tracking procedures. The first step, coarse space/time acquisition, searches over the large initial time and spatial uncertainties and makes coarse estimates of downlink time and satellite location. Because of the large initial uncertainties, the coarse acquisition procedure has the potential to be very long. To allow a fast detection, the coarse acquisition procedure utilizes the low hop rate (LHR) coarse synchronization pulse and allows an initial acquisition to be made through the sidelobes as well as the mainlobe of the ASCAMP antenna. The LHR sync pulse has a longer duration than the high hop rate (HHR) sync pulse so that fewer time hypotheses are needed to cover the large time search window. It also has a higher energy content so that detection can take place with a single hop accumulation. The time to perform coarse acquisition may be as short as 13 s and increases as a function of the initial time uncertainty. At the completion of coarse acquisition, timing accuracy is reduced to $T_{\text{LHR}}/4$ and pointing uncertainty to ±0.7°.

If coarse acquisition fails to result in a detection, the terminal must have a fallback acquisition mode. The fallback mode in ASCAMP gives the user the option to manually alter the timing and/or pointing parameters by changing the downlink time, opening the time uncertainty window, changing the location information, releveling the antenna, selecting a different satellite, etc. After making the desired changes, the user restarts the nominal coarse acquisition procedure.

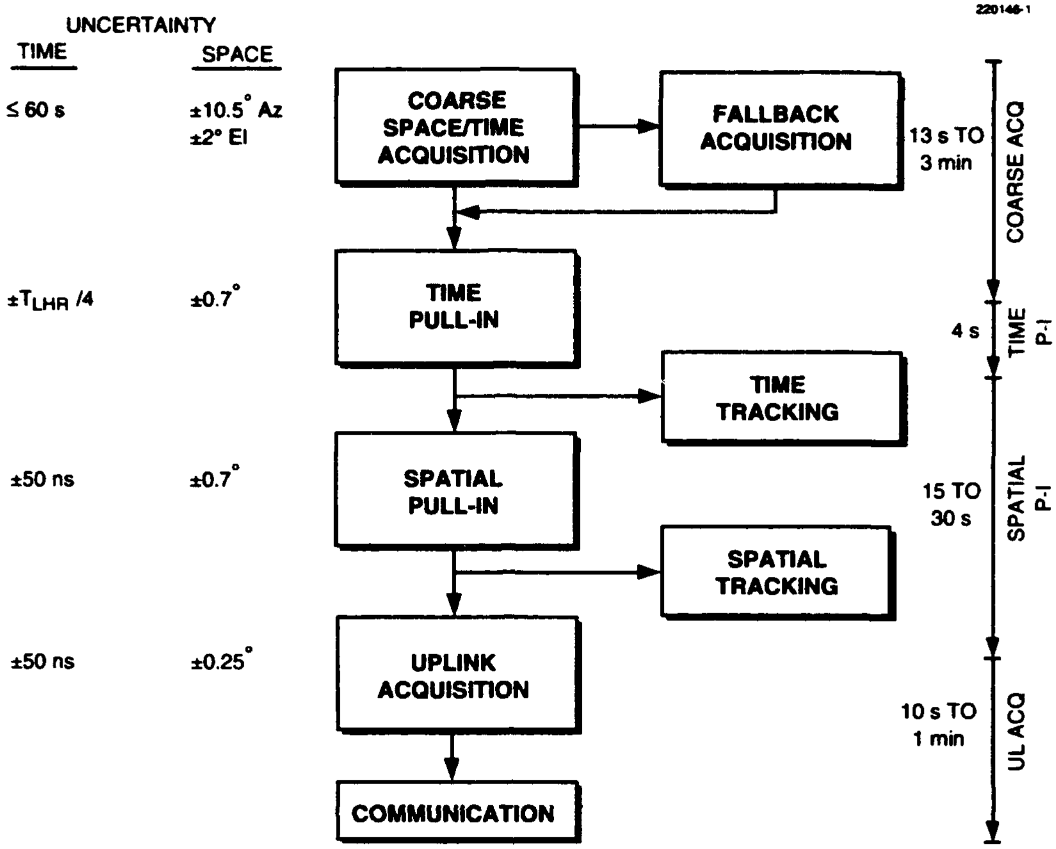

Figure 1. Acquisition and tracking sequence.

Time pull-in automatically follows coarse acquisition and is designed to reduce time uncertainty from $T_{\mathrm{LHR}}/4$ to 50 ns. It consists of a three-step pull-in procedure, where each step has a unique signal processing and control algorithm. Time tracking is an extension of the third time pull-in step and is performed continuously until the terminal is shut off.

Spatial pull-in begins in conjunction with the start of time tracking. It reduces the pointing uncertainty with progressively finer adjustments to the pointing offsets. Spatial tracking is divided into two parts—open-loop and closed-loop. Open-loop spatial tracking regularly updates (a_t, e_t) based on ephemeris calculations and corrects the pointing hypothesis. Closed-loop spatial tracking occurs less frequently and refines (Δa, Δe) based on P_r/N_0 measurements made at dither angles on either side of the pointing hypothesis. The HHR coarse synchronization pulse is used to make the P_r/N_0 estimates because it is less sensitive to timing jitter than the HHR fine sync pulse. The combination of open-loop and closed-loop spatial tracking procedures results in a pointing accuracy of 0.25°.

The minimum time to perform the steps from acquisition to communication is 42 s using FEP satellites (somewhat longer when using Milstar). This time increases as P_r/N_o is reduced, time uncertainty is increased, or the number of terminals in contention for satellite resources is increased.

1.4 FRONT-END SIGNAL PROCESSING

The ASCAMP front-end demodulator, shown in Figure 2, is the first stage of the receiver hardware and is used for all acquisition and communication modes. The signal processing steps that follow the front end are different for each of the acquisition and tracking modes and are described elsewhere in this report. The digital receiver design [2,3] utilizes a hard-limiter to simplify the hardware and to eliminate the need for automatic gain control circuitry.

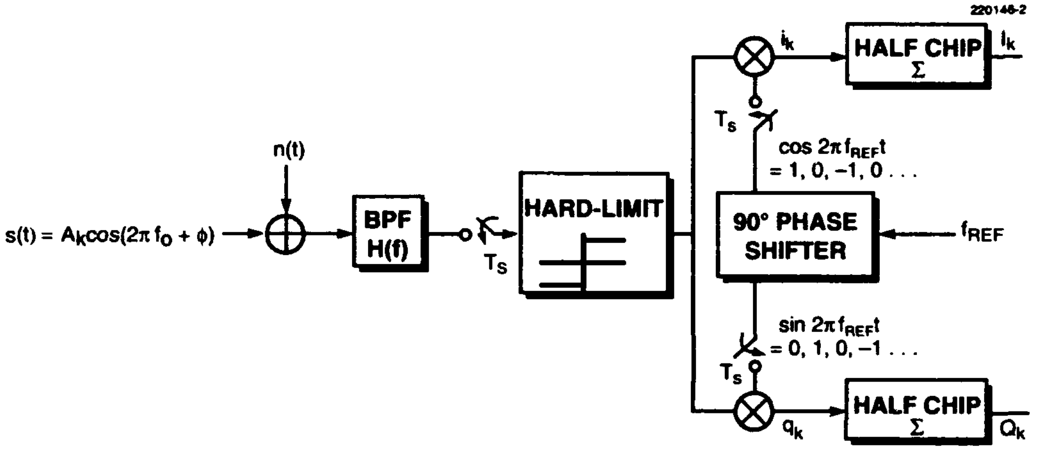

Figure 2. ASCAMP front-end receiver.

The received intermediate frequency signal $s(t)$ is modeled as a sinusoidal waveform given by the equation

$$s(t) = A_k \cos[2\pi f_0\, t + \phi], \tag{5}$$

where A_k is the amplitude and sign of the signal for chip period k (duration T_C) and ϕ is the random phase of the carrier, assumed to be constant for the duration of one hop period T_H. Because sampling occurs asynchronously with respect to the carrier phase, ϕ is random from one hop to the next. The received signal is assumed to be contaminated by additive white Gaussian noise $n(t)$. The received sync pulse is passed through a bandpass filter centered at frequency f_o. The message signal is assumed to be unchanged by the filter while the noise is colored and assumed to be Gaussian with probability density given by

$$P_n(n) = \frac{1}{\sigma_n\sqrt{2\pi}} e^{-n^2/2\sigma_n^2} \ . \tag{6}$$

The ASCAMP filtering process consists of three separate stages of bandpass filtering in the low noise amplifier and downconvertor with a mixing stage between each filter. The first stage is a three-pole Chebyshev filter with nominal center frequency of 1.478 GHz and half-power bandwidth of 74 MHz. The second stage is a four-pole Chebyshev filter with center frequency of 130 MHz and bandwidth of 10 MHz. The third stage is a single-pole LRC filter with 3-dB bandwidth equal to 4 MHz at the final 30-MHz center frequency. The measured response of the ASCAMP receiver has been modeled in the passband by

$$[\ |H(f)|^2] = 10^{-0.0389\left(|f|-f_c\right)^2} \qquad \text{for } -\infty < f < \infty \ , \tag{7}$$

where $f_c = 30.25$ MHz and f is in megahertz. By using this model of $H(f)$, the noise bandwidth of the ASCAMP filter is calculated as

$$B_N = \int_0^\infty |H(f)\ |^2 df = 5.92\ \text{MHz} \ . \tag{8}$$

The filtered signal is sampled at time intervals selected from the possible set

$$T_S = \frac{1}{4f_0} \times (1,3,5,\cdots) \tag{9}$$

so that the sampled sequence corresponds to

$$\ldots,\ A_k\cos\phi + n_0,\ A_k\sin\phi + n_1,\ -A_k\cos\phi + n_2,\ -A_k\sin\phi + n_3,\ \ldots, \tag{10}$$

where n_i is the sample of the filtered noise signal at time $t = iT_S$. Every other sample in this sequence has identical but negative expected value while the expected values of alternating samples have a quadrature relationship in ϕ. The sampling rate, $1/T_S$, is chosen much higher than the chipping frequency, $1/T_C$, to ensure that a large number of samples are made for each chip period.

The sampled sequence is hard-limited to values of ±1 prior to being separated into an in-phase (I) and quadrature (Q) component. The quadrature separation is achieved by multiplying the sample sequence by reference oscillator signals with a 90° phase shift between the I and Q channels. The frequency of the reference oscillator is selected as one of the frequencies given by

$$f_{\text{REF}} = \frac{1}{4T_S}(1,3,5,\cdots) \tag{11}$$

so that the oscillating signals at the sampling instants are exactly equal to shifted versions of a 1, 0, −1, 0, ... sequence. After the hard-limited sequence is multiplied by the oscillating signals, the i_k and q_k sequences that result are given by

$$i_k\text{: ..., sgn } (A_k\cos\phi + n_0),\ 0,\ -\text{sgn } (-A_k\cos\phi + n_2),\ 0,\ ... \tag{12}$$

and

$$q_k\text{: ..., } 0,\ \text{sgn } (A_k\sin\phi + n_1),\ 0,\ -\text{sgn } (-A_k\sin\phi + n_3),\ ...\ . \tag{13}$$

Because the zero values contain no information, the relevant portion of the i_k and q_k sequences may be exactly represented by a single bit denoting the sign of the demodulated sample. Furthermore, all the nonzero i_k or q_k bits are identically distributed. As a final step the front end adds the i_k and q_k samples over half a chip period, N nonzero samples, to give the front end outputs I_k and Q_k.

1.5 FRONT-END SIGNAL STATISTICS

Although the hard-limiter simplifies the hardware, it causes the front-end outputs to saturate for moderate signal-to-noise ratio (SNR), making linear models invalid and analysis cumbersome. For an equivalent receiver with no hard-limiter, $E[I_k]/N$ and $E[Q_k]/N$ would be directly related to $A_k\cos\phi/\sigma_n$ and $A_k\sin\phi/\sigma_n$. Traditional detection methods could be used and would eliminate any dependence on ϕ. The hard-limiter, however, changes the statistics of I_k and Q_k, resulting in a complicated, nonlinear dependence on the SNR and phase given by

$$\frac{E[I_k]}{N} = \sqrt{\frac{2}{\pi}} \int_{-\frac{A_k}{\sigma_n}\cos\phi}^{\infty} e^{-n^2/2} dn - 1 \tag{14}$$

and

$$\frac{E[Q_k]}{N} = \sqrt{\frac{2}{\pi}} \int_{-\frac{A_k}{\sigma_n}\sin\phi}^{\infty} e^{-n^2/2} dn - 1\ . \tag{15}$$

This relationship is illustrated in Figure 3, where $E[I]/N$ saturates for moderate values of $A_k\cos\phi/\sigma_n$. This channel saturation leads to nonlinear acquisition discriminants that have significant variations at high P_r/N_o due to phase dependence. These characteristics present a problem for the spatial tracking procedure and are discussed further in Section 4.

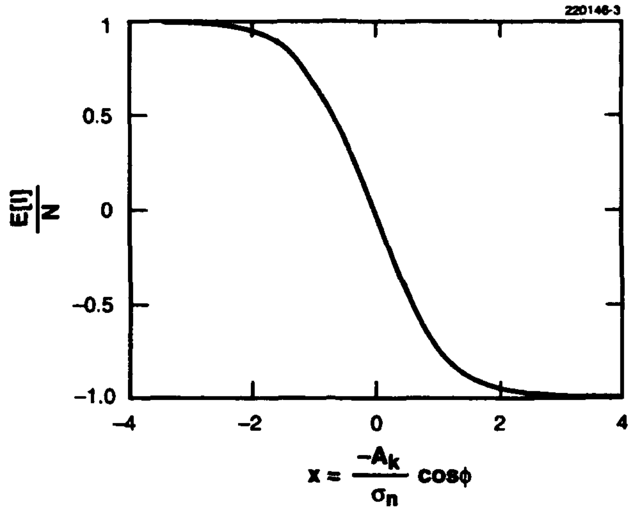

Figure 3. Saturation of front-end outputs.

2. COARSE SPACE/TIME ACQUISITION

2.1 OVERVIEW

The first step of the downlink synchronization and pointing procedures is coarse acquisition. It is divided into separate time and spatial acquisition steps as shown in Figure 4. During coarse time acquisition, the terminal scans the space and time uncertainty windows just until it detects the arrival of an LHR coarse sync pulse and synchronizes the downlink clock. It achieves the desired acquisition performance in three steps—energy detection, false alarm rejection, and sync pulse verification. Energy detection performs a threshold comparison with a low energy threshold, selected near the noise floor, to detect signals received in sidelobes as well as the mainlobe of the ASCAMP antenna. Because a large number of false alarms is expected due to noise energy, the more selective false alarm rejection (FAR) algorithm is used. It compares the string of energy crossings to the expected form of the sync pulse and eliminates potential false detections due to noise energy. Sync pulse verification confirms the initial detection by repeating the energy detection and FAR algorithm for a reduced time window.

Synchronizing in sidelobes reduces the fraction of the spatial uncertainty window that is searched prior to detection; however, it must be followed by an additional spatial acquisition step so that communication is not established through a sidelobe. With a reduced time uncertainty window, ASCAMP performs coarse spatial acquisition by scanning the region around the initial detection and pointing the antenna so that the mainlobe is aimed toward the satellite. Spatial acquisition searches first in azimuth and pulls-in from as far as the third sidelobe. If the energy from the azimuth scan is not high enough to indicate that the signal is being received through the mainlobe, then a second mainlobe search is automatically performed in elevation.

2.2 SIGNAL PROCESSING FOR COARSE ACQUISITION

Although ASCAMP is an HHR communication terminal, the LHR coarse sync pulse is used for detection during coarse acquisition. When compared to the HHR sync pulses, its longer duration allows time hypotheses to be more widely spaced throughout the time uncertainty window, and its higher energy content allows decisions to be made with a single accumulation.

The demodulator uses I_k and Q_k front-end outputs corresponding to quarter-hop accumulation periods and forms correlation outputs Δ_j, that are generated for time hypotheses spaced by a quarter-hop period. The Δ_j values are loosely referred to as "energy" outputs although they do not precisely represent the signal energy due to the hard-limiter. Each output combines four consecutive I_k's and Q_k's to give a measure of the correlation between the received signal and the expected LHR sync pulse according to the equation

$$\Delta_j = \frac{1}{4{,}096}\left\{\left(a_0 I_j + a_1 I_{j+1} + a_2 I_{j+2} + a_3 I_{j+3}\right)^2 + \left(a_0 Q_j + a_1 Q_{j+1} + a_2 Q_{j+2} + a_3 Q_{j+3}\right)^2\right\} , \quad \text{for } j = 4, 5, \cdots, 4T_{\text{SEARCH ACQ}} / T_{\text{LHR}} . \tag{16}$$

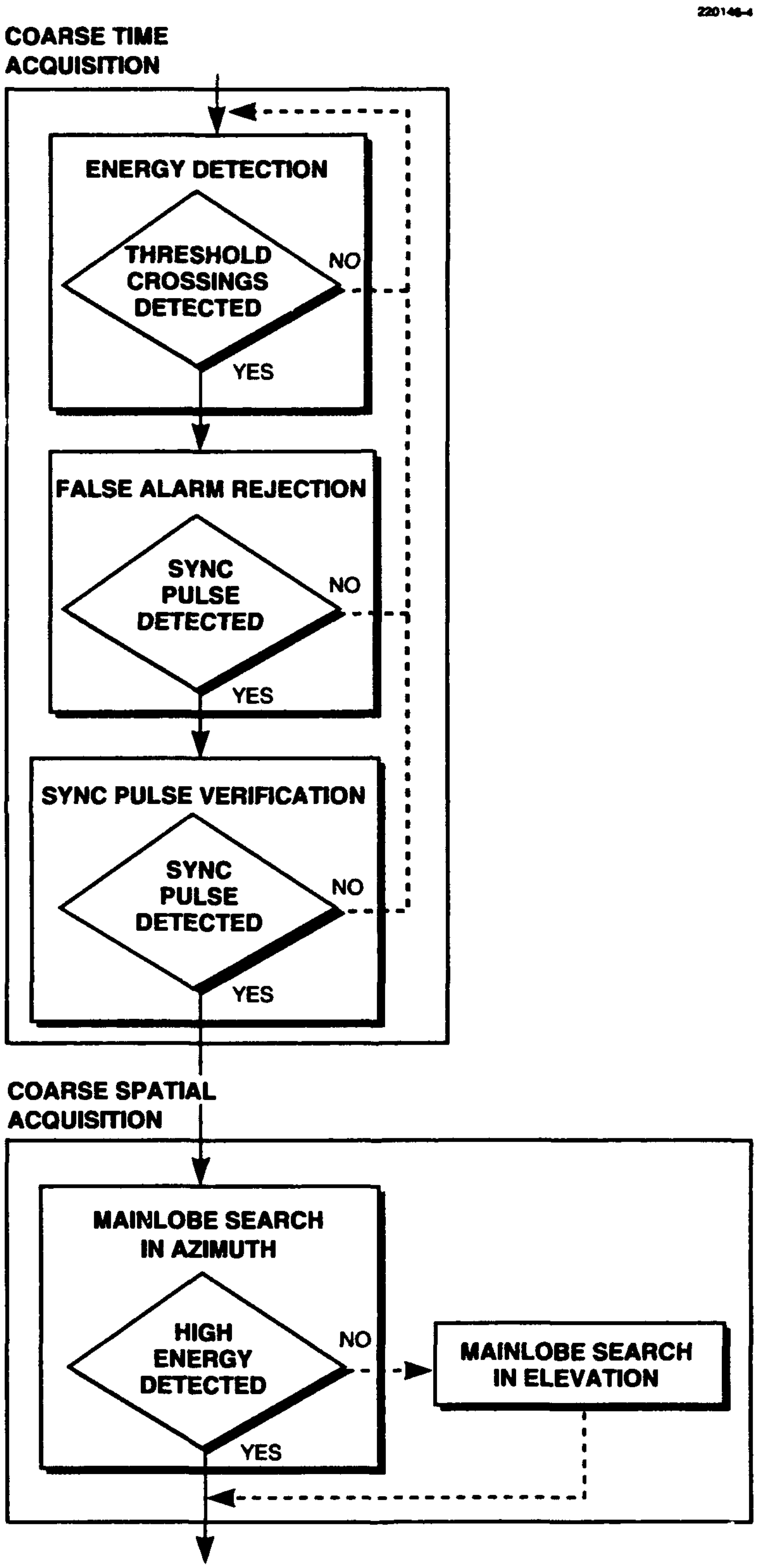

Figure 4. Flow chart of coarse acquisition.

The 1/4096 scale factor allows the dynamic range of outputs to fit into 16 bit registers and has negligible effect on the performance. Both the squaring and scaling operations are implemented in a lookup read-only memory (ROM). Because four or five consecutive I_k and Q_k sums contain sync pulse energy, seven or eight consecutive Δ_j values are affected by the presence of a sync pulse. The Δ_j output sequence, however, has considerable variation due to timing errors, random noise, and differences in received P_r/N_o and phase angles.

Figure 5 illustrates the nominal best and worst cases of output sequences due to differences in time errors. The best case has a single peak output value corresponding to a time hypothesis with no time error. The worst case has two equal but considerably lower peak outputs corresponding to time errors of $\pm T_{\mathrm{LHR}}/8$. The magnitudes of the output values depend on the received P_r/N_o and carrier phase.

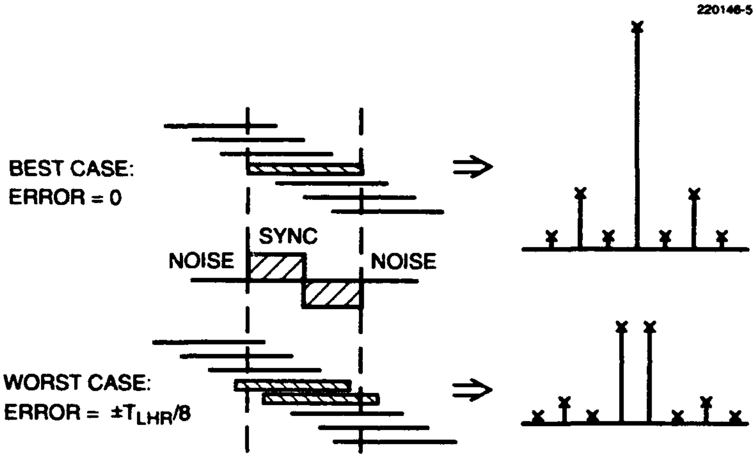

Figure 5. Output sequences for processed sync pulse.

Figure 6 shows the measured range of the peak correlation outputs as a function of P_r/N_o for the operating region of 55 to 75 dB-Hz. The data measured for each P_r/N_o is taken for uniformly distributed time errors from $-T_{\mathrm{LHR}}/8$ to $+T_{\mathrm{LHR}}/8$ and random phase angles. Theoretically, the maximum output corresponds to zero time error and phase angles of 45°, 135°, 225°, or 315°, where the I_k and Q_k channels have identical statistics. The minimum peak output corresponds to a sequence with errors of $\pm T_{\mathrm{LHR}}/8$ in the best time hypotheses and a phase angle of 0°, 90°, 180°, or 270°, where either I_k or Q_k has a zero expected value. The threshold for energy detection is selected independently of P_r/N_o so that at least three threshold crossings are expected when a sync pulse is present over the entire range of operating conditions. The FAR algorithm, however, uses a secondary threshold based on the measured peak output, thereby adapting the detection sensitivity to the received P_r/N_o.

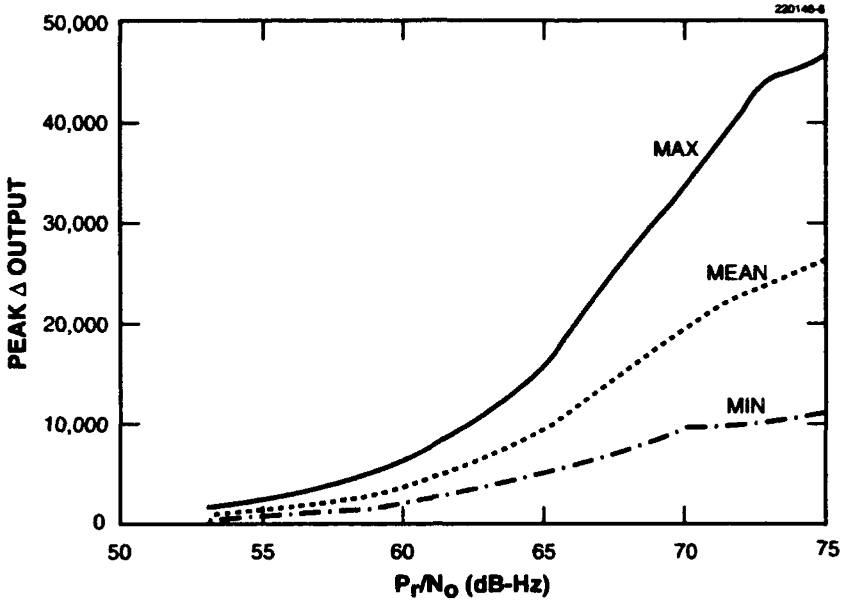

Figure 6. Peak output versus P_r/N_o.

2.3 ACQUISITION PROCEDURES

The coarse acquisition procedure steps through the spatial uncertainty window and searches the time window to determine the point in space and time that gives the maximum energy output.

2.3.1 Partitioning the Acquisition Search Windows

The nominal spatial search window for coarse time acquisition is defined as shown in Figure 7 with dimensions 21° in azimuth and 1.4° in elevation and the spatial hypothesis, s_o, located at its center. It is divided into 15 spatial cells with width and height equal to the ASCAMP receive half-power beamwidth (HPBW) of 1.4°. Energy detection begins in the center cell and moves sequentially outward to the right, then returns to the center and moves outward to the left.

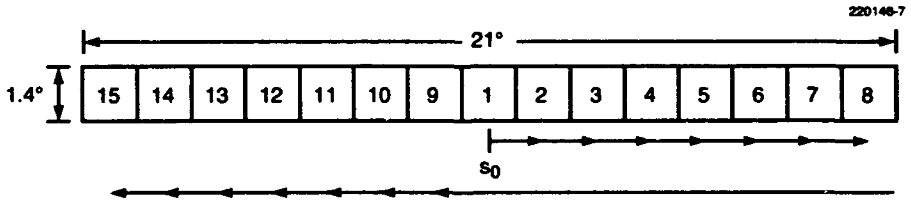

Figure 7. Spatial search window.

If the time search window is greater than 7.5 s (a limit set by the ASCAMP acquisition memory allotment), it is partitioned into smaller segments referred to as "time slices," as shown in Figure 8. The time slices overlap so that signals near the edge will not be missed due to uncompensated timing drifts. During coarse time acquisition all the time slices are searched in one spatial cell before moving on to the next spatial cell to minimize antenna motion. Time slices are always searched in the same order, starting in the center of the time search window and zig-zagging outward. Once an initial synchronization occurs, the time uncertainty window is reduced so that the remainder of the search only requires one short time slice.

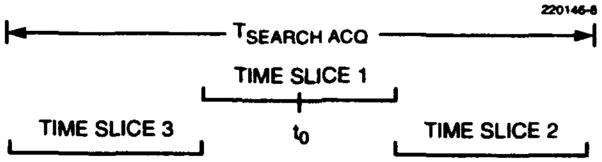

Figure 8. Time search window.

2.3.2 Philosophy of Sidelobe Detection

The receive gain pattern of the ASCAMP antenna [4] is shown in Figure 9 and is characterized by distinctive sidelobes. These sidelobes, together with a wide range of operating conditions, make it difficult to use a traditional acquisition procedure, i.e., one that compares the energy outputs to a high detection threshold selected between the level for the sidelobes and the mainlobe. Instead, by using a low energy threshold ASCAMP allows for an initial acquisition through sidelobes and increases the region for acquisition success, reducing the average number of spatial cells that must be searched as well as the total acquisition time.

2.3.3 Coarse Time Acquisition

Coarse time acquisition is the initial synchronization procedure and can succeed through either a sidelobe or mainlobe of the ASCAMP receive antenna pattern. Its objective is to quickly and reliably reduce the time uncertainty to a quarter of an LHR hop period and is accomplished in three steps: energy detection, false alarm rejection (FAR), and sync pulse verification.

Energy Detection. During energy detection, the terminal points to the center of each spatial cell, sets the downlink clock to the beginning of the desired time slice, and calculates the energy threshold Θ_E as a function of the time slice T_S (not necessarily equal to the time search window) according to

$$\theta_E = 89 + 15 \log T_S \quad . \tag{17}$$

After the Δ_j outputs are processed for a complete time slice, a threshold comparison is made in hardware between all the correlation outputs and Θ_E. This procedure results in a string of energy threshold crossings, E_i, and times of occurrence (in units of quarter hop intervals), t_i, that are stored in a shared memory in the form

$$(E_1, t_1), (E_2, t_2), \ldots, (E_m, t_m) \ . \tag{18}$$

They can subsequently be read by the terminal controller to complete the detection algorithm.

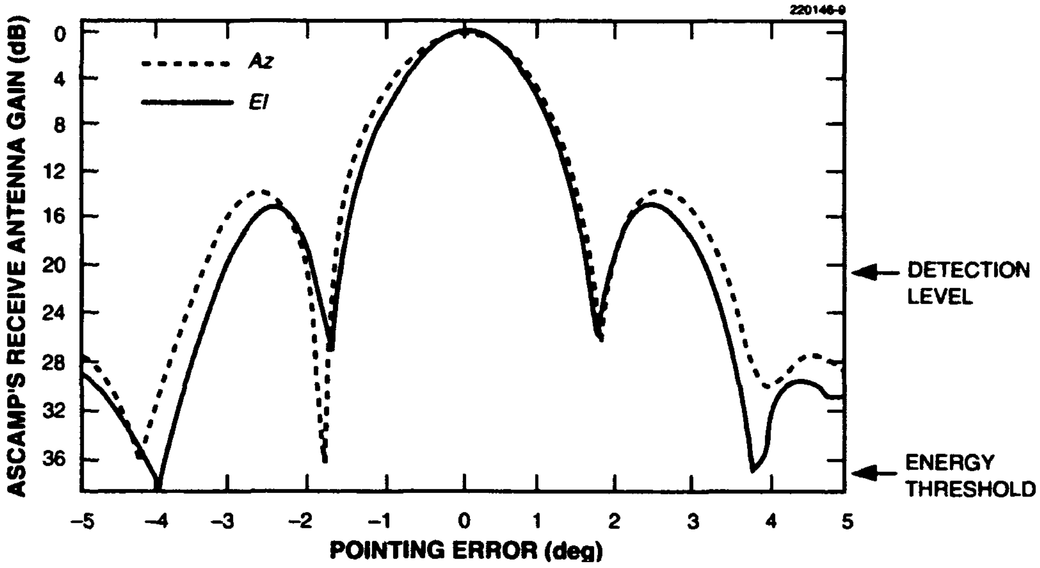

Figure 9. Receive pattern for 2-ft petal antenna.

FAR Algorithm. This algorithm is the second step of the detection procedure and is designed to eliminate false alarms resulting from the low energy threshold and to detect the sync pulse. The threshold is set low enough so that a sync pulse should result in a cluster of three to eight threshold crossings in the span of two hop periods. Processed noise, however, typically results in clusters of one or two threshold crossings. The FAR algorithm is designed to recognize a cluster of three or more crossings as a sync pulse. For each threshold crossing, the FAR algorithm determines a "power" estimate based on the "energy" per unit of time corresponding to three consecutive threshold crossings. The resulting power sequence is given by

$$P_i = \frac{E_i}{t_{i+1} - t_{i-1}}, \textit{for } i = 2, \cdots, M-1. \tag{19}$$

(If fewer than three energy crossings are observed, they are automatically assumed to be noise and the FAR algorithm is not performed.) The P_i values are compared to a power threshold Θ_p to determine if they correspond to signal or noise. The power threshold

$$\theta_p = \frac{\max E_i}{5} \tag{20}$$

adapts to the received P_r/N_0 based on the peak correlation output, denoted by max E_i. If any P_i values are above Θ_P, a detection is declared and a new time hypothesis is selected to correspond to the power crossing with the largest associated energy value E_i. False acquisitions using the FAR algorithm require that a tight cluster of three or more noise outputs exceed the energy threshold, which is selected so that the false alarm rate in the algorithm is approximately 1 per 100 time slices regardless of time slice duration.

Example of Energy Detection and the FAR Algorithm. Examples of energy detection and the FAR algorithm are shown in Figures 10 and 11. The sync pulse contributes energy to hypotheses 8 through 15 of Figure 10 and causes energy threshold crossings for hypotheses 9, 11, 12, and 14. Processed noise causes threshold crossings for outputs 2, 3, 19, and 21. The eight threshold crossings yield six P_i values shown in Figure 11, of which only two are above the power threshold Θ_P. The two associated energy values from quarter-hop periods 11 and 12 indicate that the new time hypothesis corresponds to the 12th output.

Sync Pulse Verification. The sync pulse verification stage provides an effective way of reducing the false acquisition rate from 10^{-2} to 10^{-5} in less than 1 s. Without moving the antenna from the position where the FAR algorithm succeeded, the terminal performs a short time search with a window of $\pm 2T_{\mathrm{LHR}}$, repeating the energy detection procedure and FAR algorithm using an energy threshold set to give a probability of false alarm (P_{FA}) of approximately 10^{-3}. If the FAR algorithm is successful for this second pass then the sync pulse is confirmed and coarse spatial acquisition begins with the reduced time window. If the verify step fails, then the previous time slice is searched again so that a weak sync pulse is not overlooked. If a second pass through the time slice yields a second verify failure, then the terminal moves on to the next time slice/spatial cell to avoid continuous looping on noise.

2.3.4 Coarse Spatial Acquisition

Coarse spatial acquisition improves antenna pointing, following a sidelobe detection so that communication is established through the antenna mainlobe. Its two steps—mainlobe search in azimuth and mainlobe search in elevation—are capable of pulling-in from as far as the third sidelobe in the azimuth direction and the first sidelobe in elevation. At the completion of the procedure spatial uncertainty is reduced to ±0.7° in azimuth and elevation.

Mainlobe Search in Azimuth. The mainlobe search in azimuth searches for the satellite in six cells to the right and six cells to the left of the cell where coarse time acquisition succeeded; however, any of the cells in this region that were examined during coarse time acquisition and did not reach and/or pass the verify stage are not considered. Depending on the cell where verification occurred, the search may extend beyond the nominal search window, increasing the effective search window to ±18.9° from the initial pointing hypothesis. At the end of the search, the terminal changes the pointing hypothesis, s_o, to the center of the spatial cell where the largest single energy output is detected. The peak output from the verify stage is included so that the cell where the initial synchronization took place may also be selected as the pointing hypothesis. Elapsed time for the mainlobe search in azimuth is 13 s or less, depending on the number of cells searched. (For acquisition with the earth coverage beam, a much lower P_r/N_o is expected so that acquisition beyond the first sidelobe is improbable. The mainlobe search may be shortened by searching a smaller spatial region around the point of successful verification.)

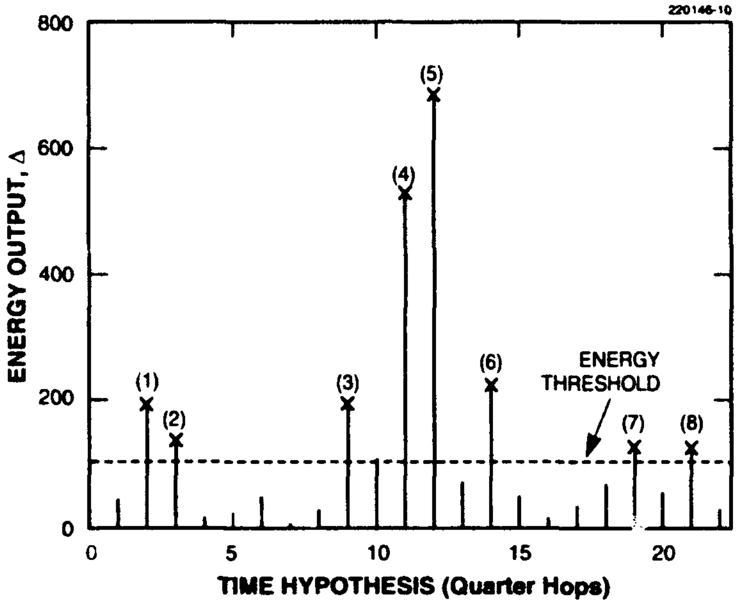

Figure 10. Example of energy detection.

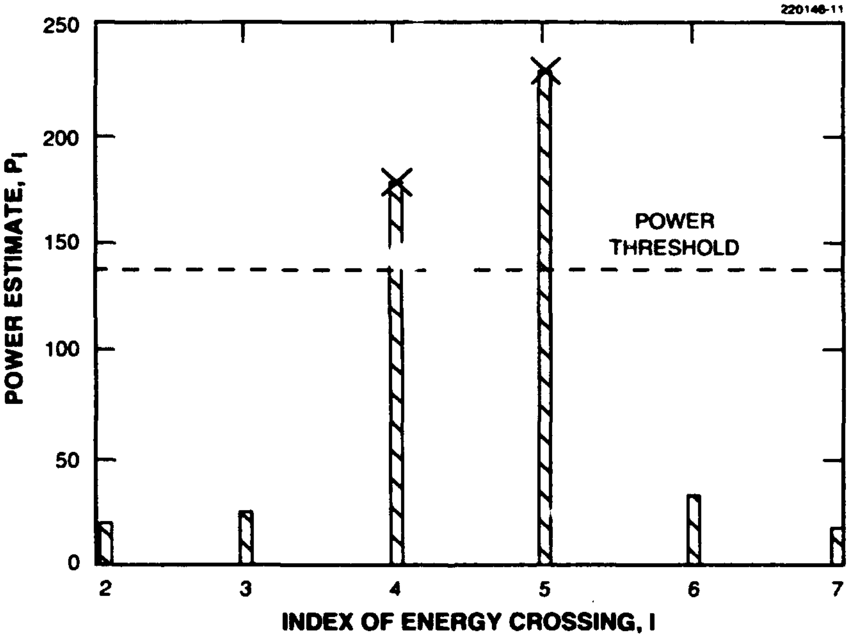

Figure 11. Example of FAR algorithm.

Figure 12 is an example of the mainlobe search in azimuth, following a coarse time acquisition in spatial cell 3. Energy is collected in 10 spatial cells, 4 through R1 and 9 through 12, skipping cells 1, 2, and 3. The largest output from each cell is compared to the peak output found in cell 3 during sync pulse verification and s_o is updated by setting the azimuth correction offset (Δa) based on the result of coarse spatial acquisition.

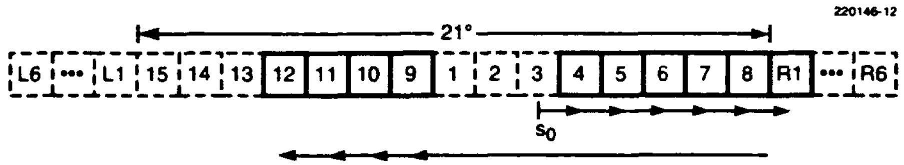

Figure 12. Mainlobe search in azimuth.

Typically, the elevation error prior to acquisition is small enough so that the pointing hypothesis at the end of the mainlobe search in azimuth aligns the mainlobe with the satellite, and any remaining pointing error will be corrected during spatial pull-in. If, however the initial elevation error is greater than 1.4° due to problems with calibration or leveling, then the satellite signal may still be received through a sidelobe and the antenna mainlobe will be pointed above or below the satellite.

Mainlobe Search in Elevation. If the peak output from the mainlobe search in azimuth is less than what is expected for a mainlobe reception, then the terminal performs a second spatial acquisition step, mainlobe search in elevation, to pull-in from the first sidelobe. The mainlobe search in elevation consists of an azimuth sweep of four spatial cells above and four spatial cells below the pointing hypothesis selected during the mainlobe search in azimuth, s_o, to correct pointing in elevation (as well as azimuth). The terminal points to the center of eight adjunct cells (labeled A through H in Figure 13) defined to accommodate the specific antenna pattern of ASCAMP. In each cell it makes one accumulation of the LHR sync pulse and records the peak correlation output. Searching the cells in alphabetical order requires the least antenna motion and adds less than 8 s to acquisition time. The eight peak outputs are compared to the peak output measured at s_o and if any are greater, then the point where the largest one was recorded becomes the new pointing hypothesis. If none of the eight measurements yields a larger energy value, then s_o remains the pointing hypothesis. By the end of the mainlobe search in elevation, the satellite signal should be received through the mainlobe, provided the initial elevation error was less than 2.8°.

2.4 COARSE ACQUISITION PERFORMANCE

2.4.1 Probability of False Acquisition

A false acquisition occurs when noise outputs cause the acquisition algorithm to falsely signal a detection. The measured probability of a false acquisition using the FAR algorithm is plotted in Figure 14 as a function of the energy threshold for a 10-ms time slice[2]. The plot shows that using the FAR algorithm reduces the P_{FA} that would have resulted from simple threshold detections. In general, larger time search windows have a greater probability of false acquisition than small windows because there is a greater number of output values that could trigger the algorithm. ASCAMP, however, selects the threshold as a function of the time slice so that $P_{FA} \approx 10^{-2}$ for all cases. The verification stage then reduces the false acquisition rate to 1 in 10^5 time slices.

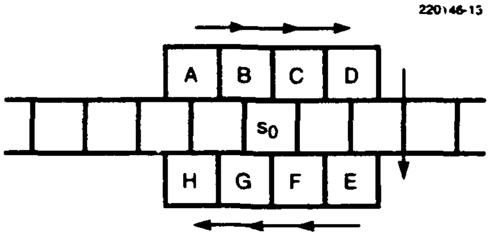

Figure 13. Mainlobe search in elevation.

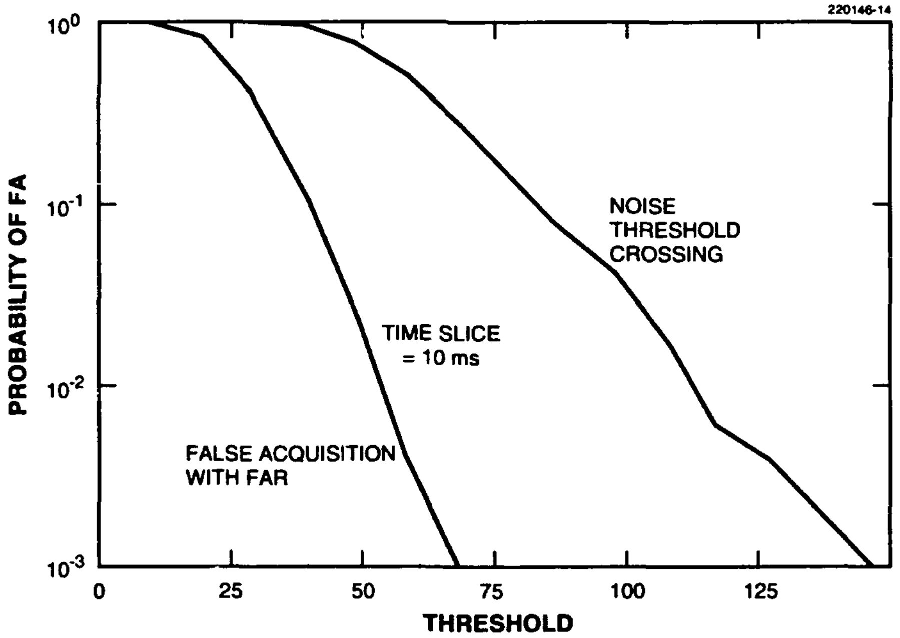

Figure 14. Probability of a false acquisition on noise.

---

[2] Although 10 ms is smaller than the minimum allowed time slice, it was a convenient test case for verifying simulation results.

2.4.2 Probability of a Missed Detection

A missed detection occurs if a sync pulse is present in the time search window but is not detected by the acquisition algorithm. Figure 15 shows the measured probability of a missed detection as a function of P_r/N_0 at the completion of the FAR algorithm. Data were measured for uniformly distributed time errors ranging from $-T_{\mathrm{LHR}}/8$ to $+T_{\mathrm{LHR}}/8$ and random phase angles. The same output data were used to show how P_{MISS} changes as the threshold is changed for the different-sized time slices. Longer time slices yield a higher probability of missed detection because they use higher thresholds. On average, the desired P_{MISS} of 10^{-3} is achieved for a P_r/N_0 of 54 dB-Hz or greater.

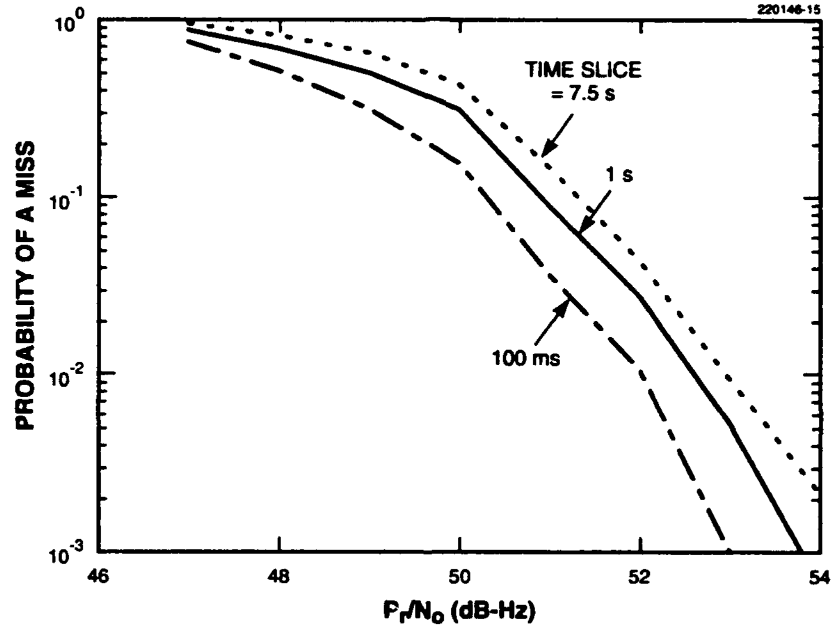

Figure 15. Probability of a missed detection.

2.4.3 Mean Time to Acquire

The mean time to acquire was calculated as a function of the acquisition time search window and the maximum received P_r/N_0 on boresight; it is plotted in Figure 16 versus the length of the time search window ($T_{\mathrm{SEARCH\ ACQ}}$). The plot relies on a model of the probability of detection versus P_r/N_0 derived from Figure 15 and assumes that the pointing error is uniformly distributed from −10.5° to +10.5° in azimuth but is zero in elevation. (The mainlobe search in elevation was not considered when calculating acquisition times.) Acquisition time increases linearly at approximately 6 times the length of the time search window and is dominated by coarse time acquisition for large search windows. Stronger links lead to a reduction in acquisition time because sidelobe detection is more probable and fewer cells are searched. Acquisition times take on discrete durations based on the period between sync pulses. For typical scenarios, acquisition from a wrist watch takes less than 1.5 min, while acquisition from the terminal standby clock takes less than 30 s.

The mean time to acquire is compared to the time to perform a conventional mainlobe acquisition. Conventional acquisition uses a high energy threshold so that an energy crossing only occurs when the antenna is pointed to the cell containing the satellite. Assuming that the timing and pointing errors are uniformly distributed, the mean time to acquire for this scheme is approximated by

$$\text{CONVENTIONAL ACQUISITION TIME} = 8.5 \times N \times T_{\text{SEARCH ACQ}} \; , \qquad (21)$$

where N indicates the number of sync pulse accumulations added prior to threshold comparison. Figure 16 shows the conventional acquisition time for $N = 1$ in comparison to ASCAMP acquisition time. For large time uncertainties and nominal P_r/N_0, the ASCAMP algorithm appears approximately 30% faster than the conventional acquisition time. In reality, the time savings with the ASCAMP algorithm are much greater. In the conventional acquisition procedure, the number of accumulations is determined in conjunction with the energy threshold to achieve the desired probabilities of false acquisition and missed detection. In practice, many accumulations are needed to meet the desired performance criteria, increasing acquisition time with each accumulation. With its low threshold and FAR algorithm, the ASCAMP algorithm can acquire with a single LHR sync pulse accumulation, allowing for great time savings. For very low P_r/N_0, the ASCAMP algorithm degenerates into the conventional mainlobe detection scheme as the detection point moves above the sidelobes and the procedure becomes comparable to a conventional mainlobe acquisition with $N = 1$.

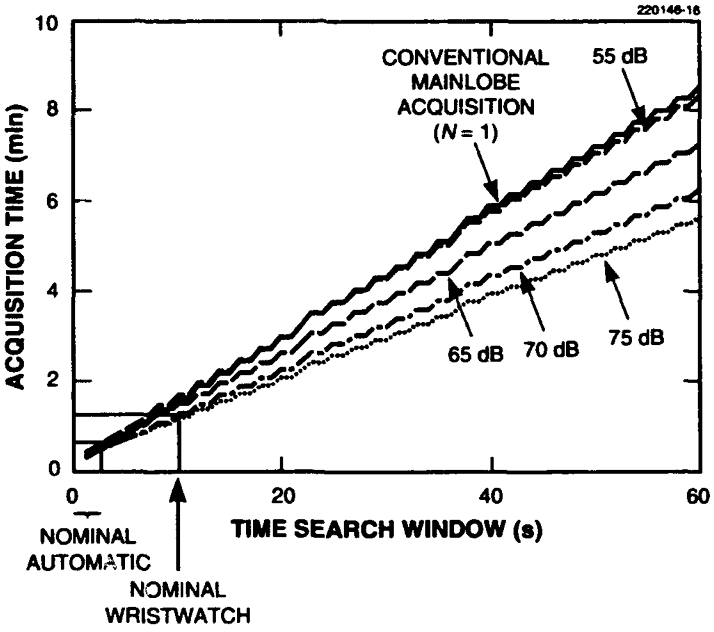

Figure 16. Mean time to acquire.

The acquisition time in ASCAMP has been reduced even further by modifying the search order of the spatial cells for coarse time acquisition. For operation with the spot beam, the effective acquisition beamwidth is larger than the 1.4° HPBW due to the ability to acquire in sidelobes. Therefore, by stepping in increments greater than one cell, the average number of points searched for coarse time acquisition is reduced. To minimize acquisition time for a 70 dB-Hz downlink signal, a three-cell step, shown in Figure 17, was implemented. The 70 dB-Hz signal results in an acquisition time equal to

$$\text{ASCAMP ACQUISITION TIME} = 3.3 \times T_{\text{SEARCH ACQ}} \quad . \tag{22}$$

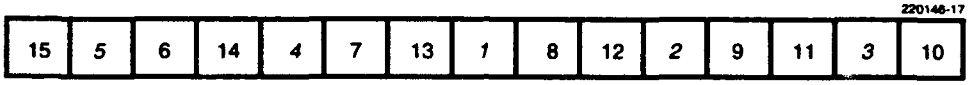

Figure 17. Three-cell search pattern.

As an example, the typical acquisition time for a 60-s time search window equals 3 min 18 s. For typical operation with time search windows less than 1 s, the nominal acquisition time is on the order of 20 s.

2.5 LINK QUALITY METRIC

The link quality metric in ASCAMP indicates the quality of the satellite-to-terminal communication path. It is defined so that a link quality of 0 corresponds to a noise signal and a link quality of 9 corresponds to a signal that is saturating the P_r/N_0 estimator. At the completion of coarse acquisition, an initial link quality estimate is made using the peak output of the LHR sync pulse. The mapping from the peak LHR output into the initial link quality estimate is defined in Table 2 and tends to give a low estimate so that subsequent link quality metrics (based on P_r/N_0 estimates) will increase after timing and pointing have been pulled in.

TABLE 2

Mapping of Initial Link Quality Estimator

Link Quality	Peak LHR Output
0	≤170
1	171 to 1800
2	1801 to 2500
3	2501 to 4500
4	4501 to 8000
5	8001 to 13000
6	13001 to 23000
7	23001 to 33000
8	33001 to 43000
9	≥43001

3. TIME PULL-IN AND TRACKING

The time pull-in procedure begins automatically after coarse acquisition and reduces the time uncertainty so that time tracking can take over and maintain the desired accuracy throughout communication. Time pull-in consists of three steps—coarse time pull-in, fine time pull-in, and final time pull-in. Coarse time pull-in uses the HHR coarse sync pulse and reduces the time uncertainty to a quarter of an HHR period. Fine time pull-in uses the HHR fine sync pulse and improves the accuracy to one one-hundredth of a hop period. Final time pull-in also uses the HHR fine sync pulse and achieves the final 50-ns time accuracy.

3.1 COARSE TIME PULL-IN

During coarse time pull-in, the downlink clock is advanced to 5 HHR hop periods before the current time hypothesis. The terminal dwells at the frequency of the expected HHR coarse sync pulse for 10 HHR hop periods, while the demodulator generates 37 output values, represented as

$$\Delta_j = \frac{1}{C}\left[\left(a_0 I_j + a_1 I_{j+1} + a_2 I_{j+2} + a_3 I_{j+3}\right)^2 + \left(a_0 Q_j + a_1 Q_{j+1} + a_2 Q_{j+2} + a_3 Q_{j+3}\right)^2\right] \quad \text{for } j = 4, 5, \cdots, 40 \tag{23}$$

and stores them in memory. Each output gives a measure of the correlation between the coarse sync pulse and the received signal for one hop period for time hypotheses spaced by a quarter of an HHR hop period. This process is repeated for 16 consecutive sync pulses while the demodulator automatically adds the correlation output values together, averaging over noise and phase angles, and stores the sums in 16 bit registers.

To keep the sum of the sync outputs from overflowing the memory locations, each output is scaled by a factor[3] *1/C selected dynamically according to Table 3. The energy discriminant used to select the* scale factor is formed by combining seven LHR outputs from coarse acquisition and is given by

$$DISC = \sqrt{1{,}024\left(\Delta_{PEAK-3} + \Delta_{PEAK-2} + \Delta_{PEAK-1} + \Delta_{PEAK} + \Delta_{PEAK+1} + \Delta_{PEAK+2} + \Delta_{PEAK+3}\right)} \tag{24}$$

where the subscripts indicate the position of the output value with respect to the peak output. If the spot beam is used for acquisition and the discriminant is greater than 4,096, then the signals for coarse time pull-in are divided by 1,024; otherwise, they are divided by 256. Figure 18 shows a plot of the measured discriminant versus P_r/N_o.

---

[3] ASCAMP software controls the magnitude of the scale via a control status table.

TABLE 3

Scaling Constant 1/C for Coarse Time Pull-In

Beam	Discriminant ≤ 4,096	Discriminant > 4,096
Spot	÷256	÷1,024
ECA	÷256	÷256

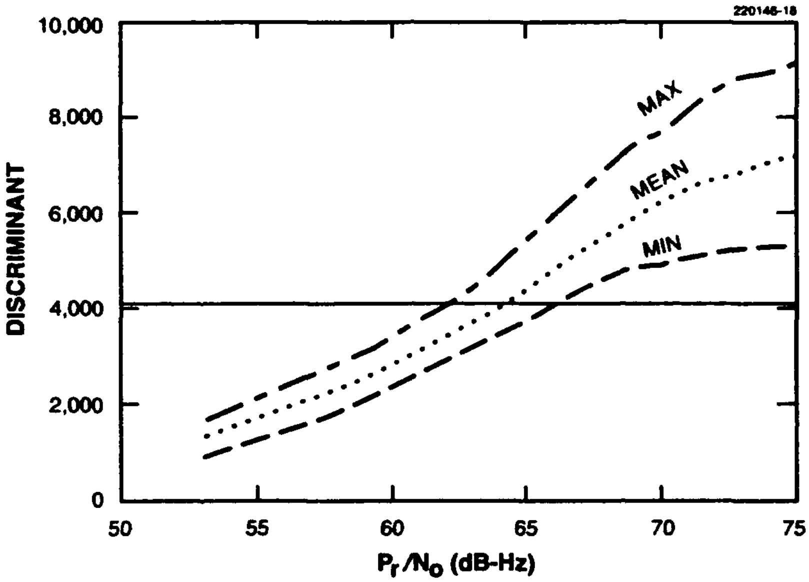

Figure 18. Range of measured discriminant values versus P_r/N_o.

After 16 accumulations have been made in hardware, the demodulator delivers all 37 correlation sums to the terminal controller and the largest is used to indicate the new time hypothesis with an accuracy of $\pm T_{\mathrm{HHR}}/4$. The peak sum is compared to a threshold to ensure that the peak value is not a noise output. If the peak sum is less than the threshold, then the time pull-in procedure is halted and the user is returned to a fallback acquisition mode. The time required to perform coarse time pull-in is a fraction of a second using FEP satellites.

3.2 FINE TIME PULL-IN

During fine time pull-in, the demodulator processes the HHR fine sync pulse and provides output values that measure the correlation between the received signal and the N chips of the fine sync pulse.

The downlink clock is advanced to 16 chip periods before the latest time hypothesis. The terminal dwells at the frequency of the fine sync pulse for $N + 32$ chip periods and generates 64 correlation outputs, given by

$$\mathrm{corr}(k) = \frac{1}{256}\left\{\left[\sum_{n=1}^{N} P_n\left(I_{2n+k-1} + I_{2n+k}\right)\right]^2 + \left[\sum_{n=1}^{N} P_n\left(Q_{2n+k-1} + Q_{2n+k}\right)\right]^2\right\}$$
$$\text{for } k = 0, 1, 2, \ldots, 63 \qquad (25)$$

where

N is the number of chips in the fine sync pulse

P_n indicates the phase of chip n and equals

+1 when the phase of the chip equals the phase of the carrier and

−1 when the phase of the chip is 180° out of phase from the carrier

I_j and Q_j are accumulations of the i and q samples over half chip j, $j = 1, \ldots 2\,N$.

At the end of the dwell period, the demodulator writes all 64 corr(k) values to the terminal controller. In this mode, the controller must accumulate the 16 sets of correlation outputs because the demodulator automatically overwrites its processing memory with each new dwell.

A new time hypothesis is selected to correspond to the peak correlation sum and is accurate to within 1% of an HHR hop period. To avoid pulling into a noise peak, the controller compares the peak sum to a threshold before implementing the new hypothesis. If the peak sum does not exceed the threshold, then the time pull-in is halted and the user is returned to a fallback acquisition mode. Fine time pull-in takes a fraction of second to complete with FEP satellites.

3.3 FINAL TIME PULL-IN AND TRACKING

The final time pull-in procedure begins at the completion of fine time pull-in and improves time accuracy to 50 ns. Time tracking is then used to maintain this accuracy. Final time pull-in and time tracking use the same algorithm, differing only in their parameters, i.e., number of accumulations, clock adjustments, etc. The algorithm was designed to compensate for clock drifts expected for operation with regularly tuned TMXOs and satellites with low inclination geosynchronous orbits. Algorithm enhancements are also described to allow greater clock slews to be achieved.

3.3.1 Design Considerations

There are several system constraints that guide the design of the final time pull-in and tracking algorithm.

Minimum Uncertainty. The hardware design of the ASCAMP downlink clock allows adjustments to be made in multiples of 50 ns; clock corrections are made only if the time error is greater than 25 ns.

Maximum Time Drift. The tracking procedure must correct for two slowly varying sources of time drift: oscillator frequency error and changes in range delay. The working clock uses a TMXO that is specified to cause worst-case time drifts of 30 ns/s. The maximum nominal drift due to changes in range delay for operation with the FEP satellites is 60 ns/s. The tracking algorithm is designed to correct for a maximum of 100 ns/s of total drift.

One Hop Processing Window. The processing window for time tracking must be kept to one hop period so that the demodulator can process signals in adjacent hops. As a result, the signal processing of the fine sync pulse is changed from the fine time pull-in so that early and late correlation outputs are obtained within the boundary of one hop.

3.3.2 Signal Processing

For the fine time pull-in and tracking procedures, the demodulator performs a correlation between the received signal and the expected fine sync pulse over only $N-2$ of its N chips. The correlation signal corrtrack(k) may be expressed as

$$\text{corrtrack}(k)=\frac{1}{64}\left\{\left[\sum_{n=2}^{N-1}P_n\left(I_{2n+k-3}+I_{2n+k-2}\right)\right]^2+\left[\sum_{n=2}^{N-1}P_n\left(Q_{2n+k-3}+Q_{2n+k-2}\right)\right]^2\right\} \tag{26}$$

$$\text{for } k=0,1,2,3,4.$$

By eliminating the first and last chips for the correlation, five different time hypotheses can be examined within the boundaries of a single hop period without advancing or delaying the clock. Three of the five corrtrack(k) values are returned to the control processor corresponding to the time hypotheses that are

- One-half chip earlier than the current on-time hypothesis = corrtrack(1)
- Synchronized to the current on-time hypothesis = corrtrack(2)
- One-half chip later than the current on-time hypothesis = corrtrack(3)

and are illustrated in Figure 19. The demodulator processes every fine sync pulse and writes the outputs to shared memory, where they are read by the controller and accumulated into variables denoted simply by corrtrack(1), corrtrack(2), and corrtrack(3).

3.3.3 Control Algorithm

A block diagram of the time tracking system is shown in Figure 20. The error detector accumulates M correlation outputs and uses the sums to calculate an error signal, D_{DIFF}, defined by

$$D_{\text{DIFF}}=\frac{\{\alpha\times[\text{corrtrack}(1)-\text{corrtrack}(3)]\}}{\text{corrtrack}(1)+\text{corrtrack}(3)} \tag{27}$$

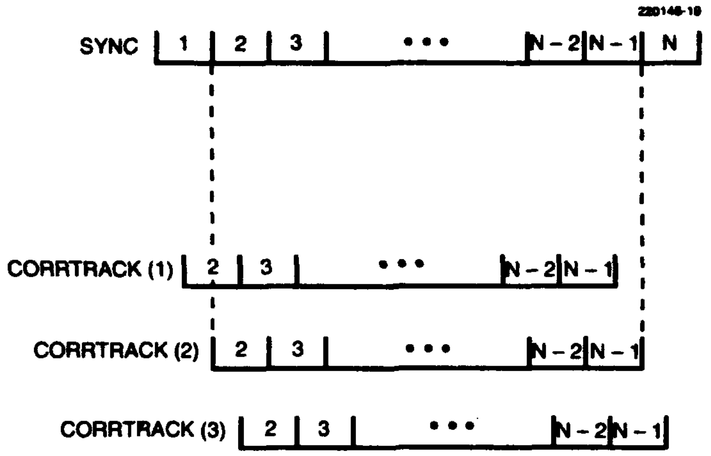

Figure 19. Time hypotheses for corrtrack outputs.

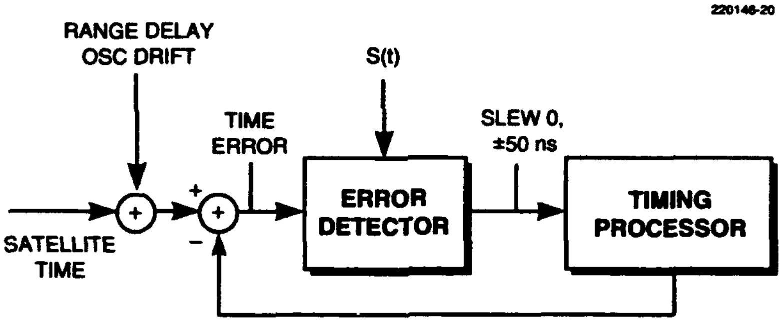

Figure 20. ASCAMP time tracking block diagram.

The scaling factor $\alpha = 256$ is selected to give adequate sensitivity to the error metric despite an integer divide performed by the ASCAMP controller. The calculated discriminant is compared to a threshold Θ_{DIFF} equal to

$$\Theta_{\mathrm{DIFF}} = E\ [D_{\mathrm{DIFF}} \mid \text{25-ns time error}]$$

to determine if the average time error over the accumulation period exceeds ±25 ns. The error detector commands the timing processor to advance or retard the clock as follows:

- $D_{\mathrm{DIFF}} > \Theta_{\mathrm{DIFF}}$ ⇒ ADVANCE
- $D_{\mathrm{DIFF}} < -\Theta_{\mathrm{DIFF}}$ ⇒ RETARD
- $-\Theta_{\mathrm{DIFF}} \le D_{\mathrm{DIFF}} \le \Theta_{\mathrm{DIFF}}$ ⇒ NO CHANGE

Figure 21 shows the error signal as a function of time error. It indicates that absolute errors as large as 1.6 μs should eventually be corrected by the tracking algorithm provided that the drift rate does not exceed 100 ns/s.

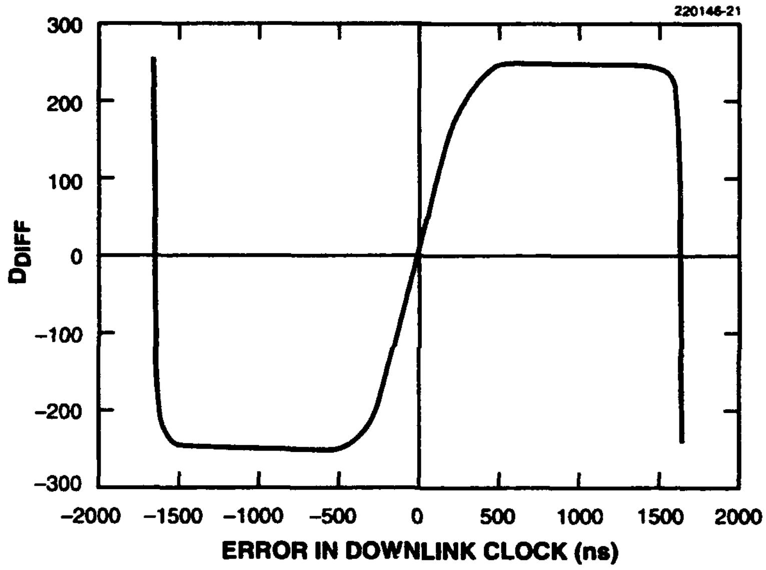

Figure 21. Error discriminant for time tracking.

The number of accumulations and the magnitude of the time adjustments to the downlink clock depend on which cycle of fine time pull-in is being performed as given in Table 4. The final time pull-in takes approximately 2 s to accumulate the sync pulses, process the sums, and slew the clock, assuming operation with FEP satellites. Final pull-in corrects for time errors up to 850 ns. Any remaining time error will be pulled in during time tracking at a maximum rate of 100 ns/s.

TABLE 4

Parameters for Final Time Pull-In and Tracking

Final Pull-In Cycle	M (No. Accum)	Time Adjustment
1	16	400 ns
2	16	200 ns
3	16	100 ns
4	16	50 ns
5	16	50 ns
6	16	50 ns
TRACKING	20	50 ns

After the sixth cycle, fine time tracking begins and continues throughout spatial pull-in, uplink acquisition, and communications. The procedure for the fine time tracking is identical to final time pull-in except that a loss-of-time tracking test is executed to identify large time errors. During each tracking cycle, the error detector determines if the average time error is greater than one-half chip period. At the end of each accumulation period, the controller checks to see if

corrtrack(1) > corrtrack(2)

or corrtrack(3) > corrtrack(2).

If this result is true for a predefined fraction of consecutive time tracking cycles, then a loss of time tracking is declared, and the terminal repeats the time pull-in procedure.

3.3.4 Time Tracking Performance

Time tracking performance was measured for various levels of P_r/N_0 and for time drifts of 0, 25, 50, 75, and 100 ns/s. The results are summarized in Figure 22. For the nominal operating P_r/N_0 of 70 dB-Hz, the data show that for drifts up to 100 ns/s, the timing accuracy is better than 50 ns. As P_r/N_0 drops, accuracy becomes worse, but the timing requirement also becomes relaxed as the terminal switches to more robust downlink communication modes. For drift rates above 100 ns/s, the tracking system is unable to keep up with the timing drift, and the downlink clock walks away for all values of P_r/N_0.

3.3.5 Enhancements for Final Time Pull-In and Tracking Algorithm

Modifications to the time tracking algorithm have been proposed for future implementation. They are intended to increase the maximum slew rate to accommodate timing drifts greater than 100 ns/s associated with less accurate oscillators or highly inclined orbits. A block diagram of the proposed system is shown in Figure 23. The error detector corrects absolute time errors in the same manner as the original tracking algorithm by accumulating fine sync correlation outputs, predicting the time error, and deciding whether to slew the clock. A second control path is added to precorrect the downlink clock for predicted, slowly varying drifts. The drift compensator is closely tied to the downlink clock and makes regular clock adjustments to compensate for drifts predicted by the correction rate that is input from the rate controller.

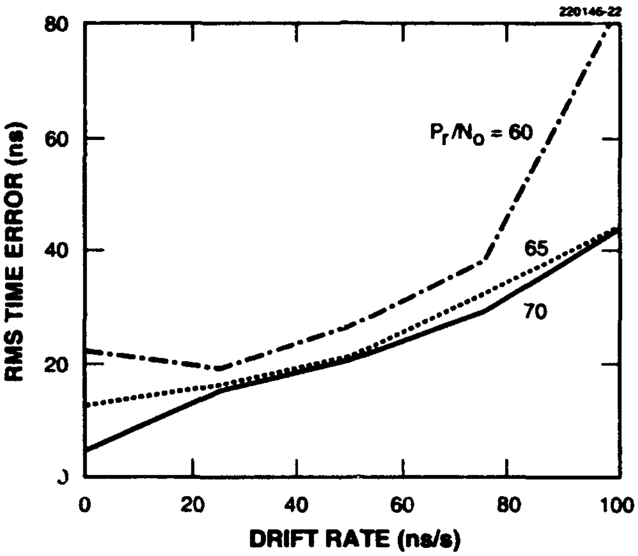

Figure 22. Time tracking performance.

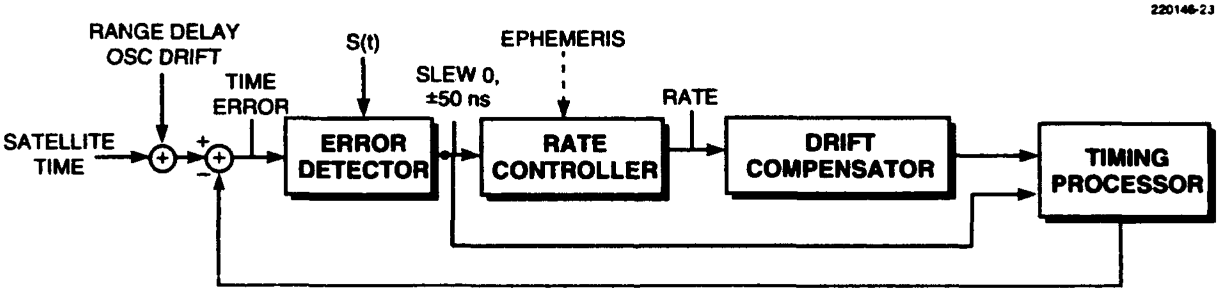

Figure 23. Modified time tracker.

The correction rate is initially set to

$$\text{INITIAL CORRECTION RATE} = \frac{1}{c}\frac{d\text{RANGE}}{dt}, \tag{28}$$

where c is the speed of light. This initial rate accounts for predicted range rates but not for oscillator-related drifts.

The pull-in sequence utilizes a final time pull-in similar to the original algorithm to reduce absolute time errors by making clock adjustments that progress from large to small. The difference is that now the drift compensator corrects for range changes at the same time, using the initial correction rate. After the final time pull-in reduces the timing accuracy, the correction rate is also pulled in using a final rate pull-in procedure, during which the error detector continues to issue clock corrections and the feedback mechanism of the rate controller is engaged. The proposed rate controller accumulates the clock slews commanded by the error detector for a specified time period, T_R, and uses them to adjust the correction rate according to the equation

$$\Delta\,\text{CORRECTION RATE} = \frac{\sum_{t=0}^{t=T_R} \text{SLEW}}{T_R}. \tag{29}$$

The final rate pull-in uses several cycles with progressively larger values of T_R to allow for finer and finer adjustments to the correction rate.

When the final rate pull-in has improved the accuracy of the correction rate, time tracking takes over and maintains the time and rate accuracies. The time tracking procedure is similar to the final rate pull-in except that the accumulation periods are changed to accommodate the long-term dynamics of the orbit.

4. SPATIAL PULL-IN AND TRACKING

4.1 OVERVIEW OF SPATIAL PULL-IN AND TRACKING

The spatial pull-in and tracking procedures point the antenna so that the satellite is located within 0.25° of the antenna boresight using open- and closed-loop correction procedures. The open-loop spatial tracking procedure is performed from power up to power down and corrects the pointing angles based on ephemeris predictions of satellite position. The closed-loop spatial tracking procedure measures differences in P_r/N_0 at symmetric dither points and uses the information to correct pointing errors. Figure 24 shows the mainlobes of the ASCAMP antenna gain curves [4]. Due to the flatness of the downlink pattern near boresight, the antenna dithers back and forth by ±0.7° to the edges of the downlink 3-dB beamwidth to make the P_r/N_0 measurements. Because the uplink loss is greater than the corresponding downlink loss, this dither is only performed when the uplink is idle. Spatial pull-in follows final time pull-in and consists of a sequence of cycles similar to closed-loop spatial tracking but with slight modifications to allow for finer and finer corrections.

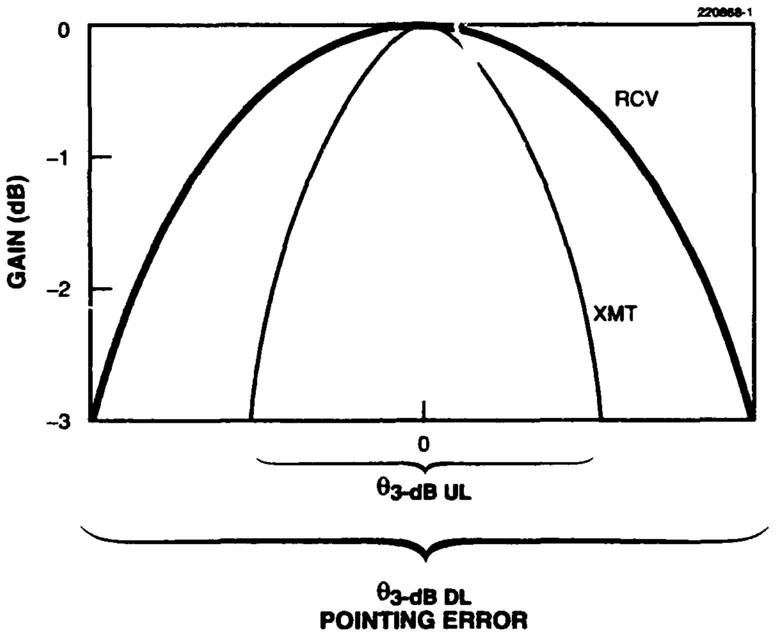

Figure 24. ASCAMP mainlobe patterns.

4.2 P_r/N_0 ESTIMATION

For P_r/N_o estimation, the receiver combines the I_k and Q_k outputs from the processed HHR coarse sync pulse for a one-hop window to form the channel signals

$$I_H = a_0 I_0 + a_1 I_1 + a_2 I_2 + a_3 I_3 \tag{30}$$

and

$$Q_H = a_0 Q_0 + a_1 Q_1 + a_2 Q_2 + a_3 Q_3 \ , \tag{31}$$

corresponding to the accumulation of identically distributed i and q samples for an entire hop period. These signals are used to recover an estimate of P_r/N_o as shown in Figure 25.

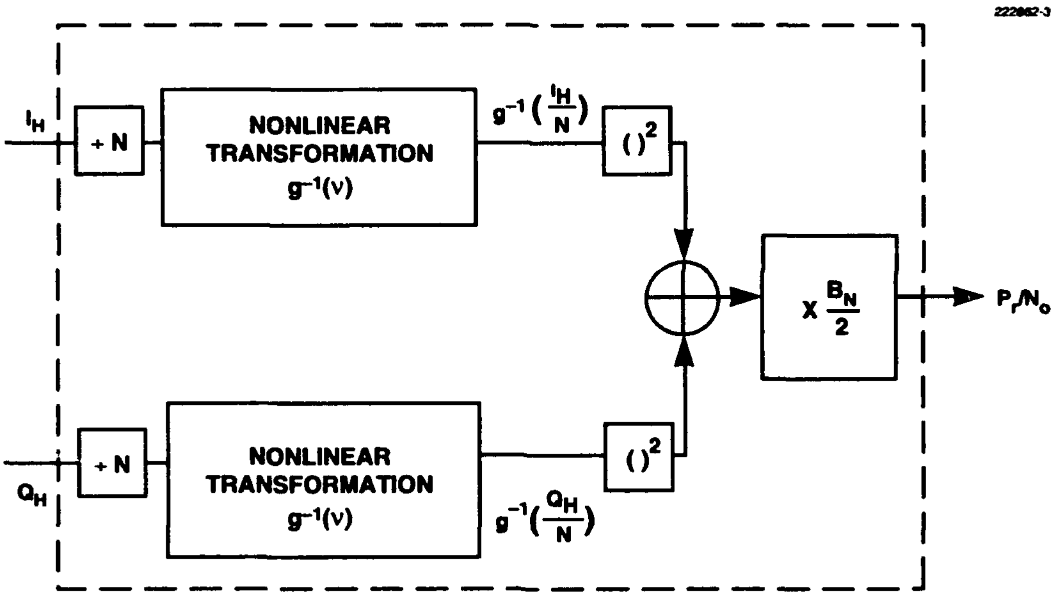

Figure 25. P_r/N_o estimation technique.

4.2.1 Theoretical Analysis of P_r/N_o Recovery

The P_r/N_o estimation technique [5] divides I_H and Q_H by the total number of nonzero i and q samples for one hop period, $N = T_H/2T_S$. The resulting channel signals have mean values given by

$$\frac{E[I_H]}{N} = g\left(-\frac{A_k}{\sigma_n}\cos\phi\right) \tag{32}$$

and

$$\frac{E[Q_H]}{N} = g\left(-\frac{A_k}{\sigma_n}\sin\phi\right) \tag{33}$$

where we define

$$g(x) = \sqrt{\frac{2}{\pi}} \int_x^{\infty} e^{-n^2/2} dn - 1. \tag{34}$$

Figure 26 compares the expected values of I_H/N and Q_H/N to the equivalent signals in a receiver without a hard-limiter. By using a multibit quantizer, the I_H/N and Q_H/N signals would be linear multiples of $A_k\cos\phi$ and $A_k\sin\phi$, respectively, so that $g(x)$ would simply be a scaling function. Subsequently, a sum of squares operation, $I_H^2 + Q_H^2$, could be used to eliminate the phase dependence and return a multiple of P_r. The hard-limiter in ASCAMP, however, makes the dependence on $A_k\cos\phi/\sigma_n$ and $A_k\sin\phi/\sigma_n$ a complicated, nonlinear relationship above moderate values of x. For ASCAMP's typical received P_r/N_o, one of the channels will be operating in the saturation region and depending on the phase angle, the second channel may also enter saturation (for ϕ near to 45°, 135°, 225°, and 315°) or it may consist of noise (for ϕ near 0°, 90°, 180°, and 270°). As a result, a sum of square operation no longer eliminates the phase dependence but causes a bimodal behavior in the P_r/N_o estimator resulting in poor estimator performance.

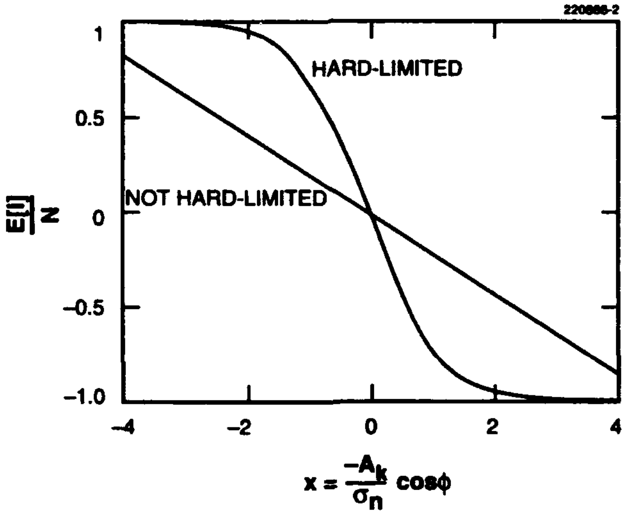

Figure 26. Comparison of $E[I_k/N]$ with and without hard-limiting.

This characteristic is compensated by relinearizing the I_H and Q_H signals to produce channel signals that more closely approximate the analog system. The demodulator performs a nonlinear transformation [6] on the normalized I_H and Q_H sums to map their expected values back into linear multiples of $A_k \cos\phi/\sigma_n$ and $A_k \sin\phi/\sigma_n$. The transformation is the inverse of $g(x)$ and results in the values

$$g^{-1}\left(\frac{I_H}{N}\right) \approx \frac{-A_k}{\sigma_n} \cos\phi \tag{35}$$

and

$$g^{-1}\left(\frac{Q_H}{N}\right) \approx \frac{-A_k}{\sigma_n} \sin\phi , \tag{36}$$

where accuracy improves with increasing N. Because P_r/N_o for a sinusoidal signal is defined by

$$\frac{P_r}{N_o} = \frac{A_k^2}{2N_o} = \frac{B_N A_k^2}{2\sigma_n^2} , \tag{37}$$

an estimate may be formed as

$$\frac{P_r}{N_o} \approx \frac{B_N}{2} \left\{ \left[g^{-1}\left(\frac{I_H}{N}\right) \right]^2 + \left[g^{-1}\left(\frac{Q_H}{N}\right) \right]^2 \right\} . \tag{38}$$

4.2.2 Implementation of P_r/N_o Estimator in ASCAMP

The ASCAMP implementation of this P_r/N_o estimator is shown in Figure 27. It uses a single lookup ROM to perform the divide by N, execute the g^{-1} transformation, square the result, and scale it. The composite lookup function is given by

$$y(\nu) = \gamma \left[g^{-1}\left(\frac{\nu}{N}\right) \right]^2 , \tag{39}$$

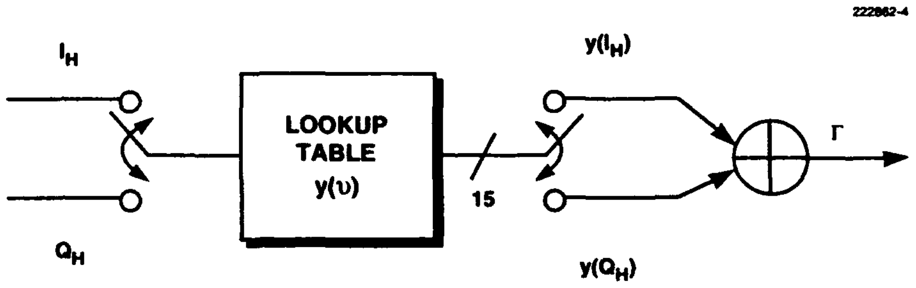

Figure 27. Implementation of the P_r/N_o estimator in ASCAMP.

where γ is a scaling constant defined so that the output fully utilizes the available dynamic range. ASCAMP sequentially uses the magnitudes of I_H and Q_H to select the appropriate ROM address and adds the outputs of the two lookup operations to give the final demodulator output,

$$\Gamma = y(I_H) + y(Q_H) \approx \frac{2\gamma}{B_N} \frac{P_r}{N_o}. \tag{40}$$

The size of the lookup table equals the total number of discrete I_H or Q_H magnitudes, $1 + N/2$, and influences the precision of the output. Because the LHR coarse sync pulse yields more samples per hop than the HHR sync pulse, it could be used to increase the precision and accuracy of Γ.

The P_r/N_o of the received signal is estimated from Γ according to the equation

$$\frac{P_r}{N_o} = \frac{B_N}{2\gamma} \Gamma. \tag{41}$$

Every 20 s, the ASCAMP controller accumulates 64 Γ outputs to determine the average P_r/N_o estimate with reduced variance due to noise, phase, and frequency hopping. The sum is used to calculate an estimate in hundredths of dB-Hz (using $B_N = 5.92 \times 10^6$ and $\gamma = 2{,}109$), according to the equation

$$\left[P_r / N_o\right]_{\text{hundredths of dB-Hz}} = 3{,}147 + 1{,}000\,[\frac{\sum_{i=1}^{M} \log \Gamma_i}{M}]. \tag{42}$$

The actual implementation in ASCAMP calibrates the estimator by using the equation

$$\left[P_r / N_o\right]_{\text{hundredths of dB-Hz}} = 3{,}011 + 1{,}036.9 \log[\frac{\sum_{i=1}^{M} \Gamma_i}{M}]. \tag{43}$$

The measured mean and standard deviation of the estimator are shown in Figures 28 and 29 for a frequency-hopped downlink signal. The 1-dB compression point is observed at an average P_r/N_o (over the hopping band) of 73 dB-Hz. Up to that point the estimator has a normal distribution and a standard deviation of 0.2 dB despite a 3-dB variation in P_r/N_o across the frequency hopping band. As the estimator saturates, its distribution becomes bimodal and the standard deviation increases. The useful operating region of the estimator can be extended to higher P_r/N_o by modifying the bandpass filter in the front end to increase the noise bandwidth for the hop periods when HHR coarse sync pulses are received.

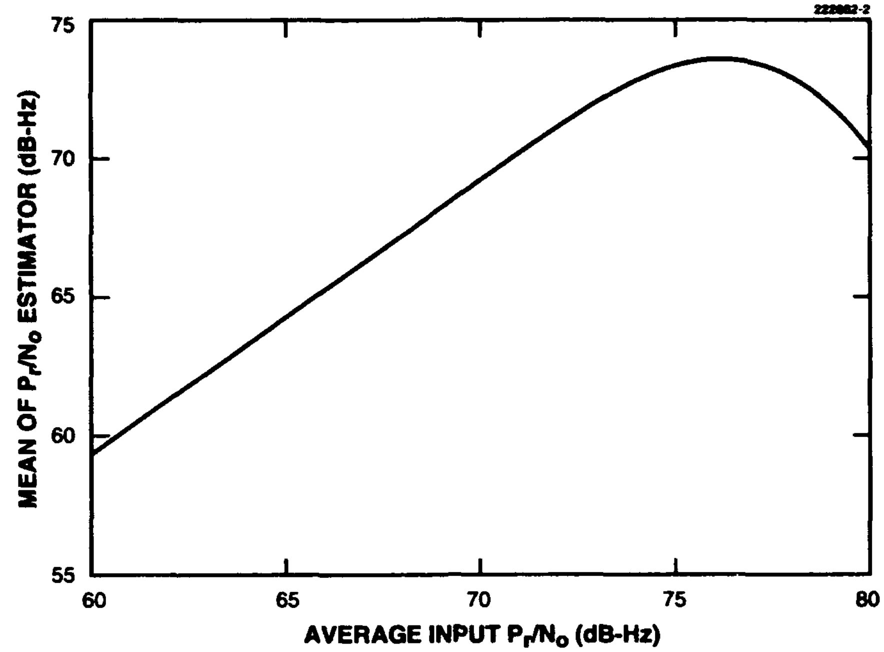

Figure 28. Mean of P_r/N_0 estimator.

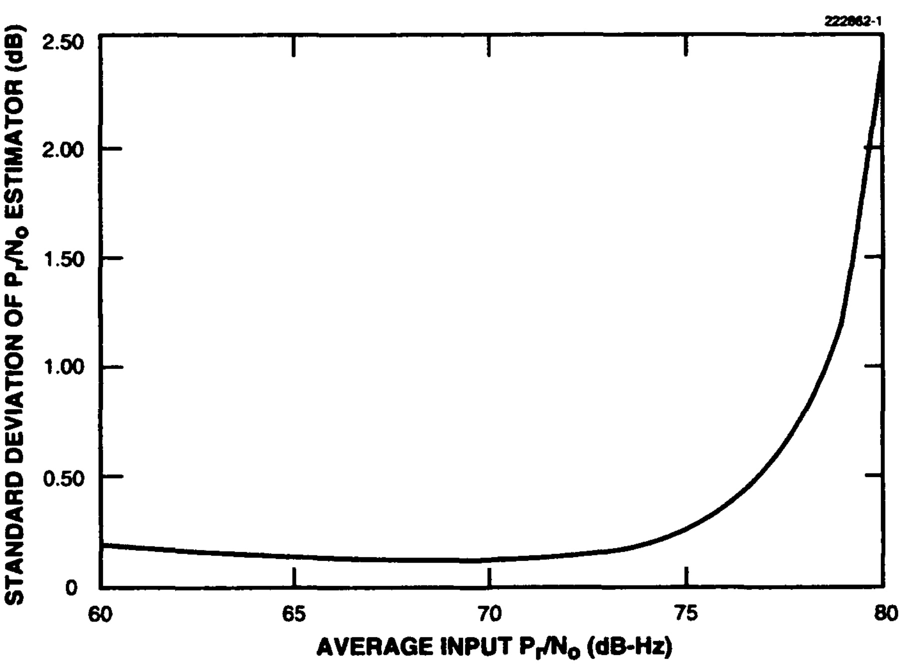

Figure 29. Standard deviation of P_r/N_0 estimator.

4.2.3 Using P_r/N_0 to Update Link Quality

Link quality is updated from the periodic P_r/N_0 estimate of the terminal according to the relationship in Table 5. The mapping between P_r/N_0 and link quality is defined so that a 3-dB increase in P_r/N_0 corresponds to an increase in link quality of 1.

TABLE 5

Definition of Link Quality

Link Quality	HHR P_r/N_0 Estimator (dB-Hz)
0	<48.99
1	49 to 51.99
2	52 to 54.99
3	55 to 57.99
4	58 to 60.99
5	61 to 63.99
6	64 to 66.99
7	67 to 69.99
8	70 to 72.99
9	>73

4.3 OPEN-LOOP SPATIAL TRACKING

The open-loop tracking procedure begins as soon as the antenna points toward the satellite to begin coarse acquisition and continues until the terminal is powered down. The terminal controller makes an ephemeris calculation every 20 s and uses the azimuth and elevation values to update the open-loop pointing angle (a_t, e_t). The new coordinates are immediately added to the stored offset angles (Δa, Δe) to determine a new pointing hypothesis. If the uplink is idle, the antenna moves to the new point; if the uplink is in use, antenna movement is delayed until it becomes idle. In the meantime, new ephemeris calculations may be made causing the pointing hypothesis to be updated again. When transmission is complete, a single pointing command is sent to reflect the most recent ephemeris angles.

The antenna controller receives the point command and adjusts the azimuth and elevation motors to the 0.05° motor step nearest the desired pointing angle. After the antenna controller has completed this procedure it sends a message to the terminal controller to convey whether the antenna has moved. Open-loop corrections are made often enough so that no more than one motor step of motion usually takes place per update for operation with low inclination orbits. Highly inclined orbits will require more frequent corrections.

4.4 CLOSED-LOOP SPATIAL TRACKING

During closed-loop tracking the antenna dithers away from the pointing hypothesis, measures the received P_r/N_o, and uses it to formulate an error signal for pointing control. If the uplink is in use or pending when a trigger condition occurs, the terminal delays the procedure until the uplink idles. In the meantime, the terminal continues to make open-loop pointing calculations. Any updates to the open-loop pointing angles are corrected when the uplink becomes idle and before closed-loop tracking begins.

4.4.1 Trigger Events

The start of closed-loop tracking is triggered by the outcome of open-loop tracking, which is monitored by two counters. First, an open-loop cycle counter (OLCC) is incremented each time that an ephemeris calculation is made to keep a record of the number of open-loop tracking cycles since the last closed-loop tracking procedure. Second, an open-loop step counter (OLSC) is incremented each time that the antenna moves in response to the open-loop update to provide a gauge for how much antenna motion has taken place.

After receiving the antenna controller move/no move message, the terminal controller updates the OLSC, reads both the OLCC and the OLSC counters, and uses their values to determine whether to start closed-loop tracking according to the trigger conditions in Table 6. If either of the trigger conditions is achieved, then the terminal begins closed-loop tracking. Nominally, a closed-loop tracking cycle is performed after the antenna moves a total of 0.2° during open-loop tracking, corresponding to the approximate pointing accuracy. The signal to indicate this trigger event is that the OLSC = 4. The time to achieve this condition with a low inclination orbit will vary from as little as 7 min to 2.5 h. To be sure that the terminal does not wait too long without a closed-loop correction, a reasonable upper bound of 20 min is imposed by detecting when the OLCC = 60 in case uplink communication has suppressed several open-loop pointing corrections.

TABLE 6

Trigger Events for Closed-Loop Tracking

Trigger Condition	Antenna moves by 0.2°	20 min elapse
Control Signal	OLSC = 4	OLCC = 60

4.4.2 Partitioning the Tracking Cycle

The closed-loop tracking procedure is broken down into separate steps to correct pointing in azimuth and elevation using identical procedures. Both are performed each time that the closed-loop tracking procedure is invoked with azimuth tracking being performed first. If the uplink is requested during either step of the operation, the terminal aborts the procedure to give priority to the transmission and resumes when the transmission is complete.

Azimuth Tracking. Before dithering the antenna, the terminal accumulates the Γ outputs at the current pointing hypothesis and stores the sum in the variable Γ_0. This accumulation is used to update the P_r/N_o estimate and the link quality. The antenna then moves to the positive dither angle, given in terminal-centered coordinates as

$$\text{POSITIVE AZIMUTH DITHER POINT} = (a_t + \Delta a + \delta,\ e_t + \Delta e) \quad . \tag{44}$$

The dither angle, $\delta = 0.7°$, equals HPBW/2 of the receive antenna. At this point, the terminal controller accumulates the Γ outputs into the variable Γ_P. The terminal then moves to the negative dither angle given by

$$\text{NEGATIVE AZIMUTH DITHER POINT} = (a_t + \Delta a - \delta,\ e_t + \Delta e) \tag{45}$$

and accumulates Γ outputs into the variable Γ_N. During the dither and accumulation procedure, open-loop pointing corrections are suppressed by ASCAMP but may be desired for operation with highly inclined orbits.

Elevation Tracking. After the azimuth tracking step the terminal immediately performs elevation tracking. If the pointing hypothesis has changed as a result of azimuth tracking, the terminal first points to the new hypothesis and reaccumulates outputs into the variable Γ_0. If the pointing hypothesis is unchanged, then the previous measurement of Γ_0 is still valid and is not repeated. Elevation tracking is identical to azimuth tracking except that the positive and negative dither points are given in terminal-centered coordinates as

$$\begin{aligned} &\text{POSITIVE AZIMUTH DITHER POINT} = (a_t + \Delta a,\ e_t + \Delta e + \delta\ ) \\ &\text{NEGATIVE AZIMUTH DITHER POINT} = (a_t + \Delta a,\ e_t + \Delta e - \delta) \quad . \end{aligned} \tag{46}$$

For both the azimuth and elevation steps, the three accumulations Γ_0, Γ_P, and Γ_N are used to predict pointing errors and determine the appropriate adjustments.

4.4.3 Critical Error Conditions

Before correcting for small pointing errors, the terminal controller checks to see if more damaging errors have occurred.

Detecting a Loss of Integrity. The first test performed assures that the antenna is not completely off in pointing and that the time synchronization is correct. During each azimuth and elevation cycle the magnitude of the positive plus negative dither accumulations ($\Gamma_P + \Gamma_N$) is compared to a threshold to be sure that it is above it for sync detection in the mainlobe. If $\Gamma_P + \Gamma_N$ is low, then either the timing or the pointing has been corrupted and the user is alerted. If this condition persists, then the terminal is returned to a fallback acquisition mode.

Detecting a Loss of Spatial Track. The second test determines if the pointing error is so large that the downlink signal is being received outside the downlink HPBW. This event is labeled "loss of spatial track" and occurs if either of the measurements at the dither angles, Γ_P or Γ_N, is greater than Γ_0. This situation corresponds to a pointing error greater than 0.7° and causes the terminal to respond by repeating the spatial pull-in procedure.

4.4.4 Nominal Error Conditions

If neither of the critical error conditions is detected, then the positive and negative accumulations are used to form an error signal and identify whether a pointing adjustment is necessary. The terminal controller forms an error signal ε that is given by

$$\varepsilon = \delta \frac{\Gamma_P - \Gamma_N}{\Gamma_P + \Gamma_N}, \tag{47}$$

where δ is a scale constant used to achieve the desired resolution despite the use of integer arithmetic.

The error signal ε is compared to two thresholds so that the terminal may respond differently for small and large pointing errors that are distinguished by the thresholds Θ_S and Θ_L, respectively. The desired response to the threshold comparisons are summarized in Table 7. A small pointing error is nominally between 0.05° and 0.25°. When detected, a small error causes a 0.1° correction to be made to the appropriate azimuth or elevation pointing offset angle. A pointing error is considered large if it is between 0.25° and 0.7°. If a large error is detected, then the terminal responds by making a 0.2° correction to the Δa or Δe offset. In addition, a large error triggers the entire tracking cycle to be repeated after the current tracking cycle has been completed. The distinction between large and small errors allows for a faster pull-in to occur when necessary without overcorrecting for errors that may be exaggerated by backlash uncertainty.

4.4.5 Time to Perform the Closed-Loop Tracking Procedure

Using FEP satellites, the combined azimuth and elevation tracking cycle takes approximately 14 s, which corresponds to the time needed to move the antenna and make measurements at six points. The period of an azimuth or elevation dither is short enough that the tracking does not compensate for temporary losses due to patchy clouds or changeable skies. With Milstar satellites the accumulation period increases and may cause atmospheric fading to become a concern.

TABLE 7

Closed-Loop Responses to Pointing Error

Error Condition	Predicted Error	Response
$\varepsilon \geq \Theta_L$	> 0.25°	Reduce pointing offset by 0.2° Repeat tracking cycle
$\Theta_L > \varepsilon \geq \Theta_S$	< 0.25°	Reduce pointing offset by 0.1°
$\lvert\varepsilon\rvert < \Theta_S$	< 0.05°	No change to pointing offset
$-\Theta_L < \varepsilon \leq -\Theta_S$	< 0.25°	Increase pointing offset by 0.1°
$\varepsilon \leq -\Theta_L$	> 0.25°	Increase pointing offset by 0.2° Repeat tracking cycle

4.5 SPATIAL PULL-IN

The spatial pull-in procedure occurs before spatial tracking and consists of five modified cycles of the closed-loop tracking procedure as summarized in Table 8. The first four cycles of spatial pull-in differ from closed-loop tracking in the number of accumulations, the magnitudes of the angle corrections to Δa and Δe, and the disabling of the critical error tests and the large error test. Only the small error threshold is used to determine whether to adjust the pointing offset. Because the two tests for critical pointing errors are disabled, no accumulation of Γ_0 is necessary. The fifth cycle of spatial pull-in is identical to a closed-loop tracking cycle and performs all the special tests and threshold comparisons. During pull-in, open-loop corrections continue to take place during the dither/accumulation maneuvers.

TABLE 8

Parameters for the Spatial Pull-In and Tracking Procedures

Cycle	M (No. Accum)	Offset Adjustment	Critical Errors/ Large Error Tests
1	32	0.4°	Off
2	32	0.2°	Off
3	32	0.1°	Off
4	32	0.1°	Off
5 and Tracking	64	0.1°	On

4.5.1 Time to Perform the Spatial Pull-In

Execution of the complete spatial pull-in procedure takes 40 s with FEP satellites; however, ASCAMP allows for a number of pull-in cycles to be skipped if they are deemed unnecessary. If the pointing error is determined to be smaller than 0.05° for both the azimuth and elevation steps in a given cycle, then the remaining cycles through the fourth are skipped. (The terminal always executes the first and the fifth pull-in cycles.) As a result, the spatial pull-in can be as fast as 18 s.

5. CONCLUSIONS

Table 9 shows the nominal setup and acquisition times for ASCAMP. The terminal can be assembled from its storage case and proceed through downlink acquisition in approximately 5 min. Downlink acquisition and pull-in procedures take approximately 1 min to execute for nominal P_r/N_0 and time search window. For acquisition with large time uncertainties, the coarse acquisition time increases. For operation with Milstar satellites, the time and spatial pull-in steps are slightly longer, but the rest remain unchanged.

TABLE 9

Summary of ASCAMP Setup Time

Base unit assembly	64 s
Antenna assembly	72 s
Parameter initialization and leveling	87 s
Satellite selection	15 s
Coarse acquisition	20 s
Time pull-in	4 s
Spatial pull-in	40 s
Total	302 s

REFERENCES

1. A. Sonnenschein, P.R. Hirschler-Marchand, and P.M. Fishman, Private communication (15 June 1990).
2. G. Gorski-Popiel, "Architecture of ASCAMP digital hardware," *1991 IEEE Mil. Commun. Conf. Rec.*, 1110–1116 (1991).
3. J. LaRocca, "Hardware implementation of the advanced SCAMP downlink processor," *1991 IEEE Mil. Commun. Conf. Rec.*, 1117–1122 (1991).
4. J.C. Lee, "A compact EHF dual-frequency antenna for ASCAMP," *1991 IEEE Mil. Commun. Conf. Rec.*, 1123–1127 (1991).
5. R.J. Figucia, "Advanced SCAMP's demodulator design for performing envelope recovery from hardlimited samples," *1992 IEEE Mil. Commun. Conf. Rec.*, 385–389 (1992).
6. E Masry and S. Cambanis, "Consistent estimation of continuous-time signals from non-linear transformations of noisy samples," *IEEE Trans. Inf. Theory*, 84–96 (January 1981).

REPORT DOCUMENTATION PAGE

Form Approved
OMB No. 0704-0188

Public reporting burden for this collection of information is estimated to average 1 hour per response, including the time for reviewing instructions, searching existing data sources, gathering and maintaining the data needed, and completing and reviewing the collection of information. Send comments regarding this burden estimate or any other aspect of this collection of information, including suggestions for reducing this burden, to Washington Headquarters Services, Directorate for Information Operations and Reports, 1215 Jefferson Davis Highway, Suite 1204, Arlington, VA 22202-4302, and to the Office of Management and Budget, Paperwork Reduction Project (0704-0188), Washington, DC 20503.

1. AGENCY USE ONLY (*Leave blank*)	2. REPORT DATE 14 September 1993	3. REPORT TYPE AND DATES COVERED Technical Report

4. TITLE AND SUBTITLE

Downlink Acquisition and Tracking Procedures for the ASCAMP
Satellite Communications Terminal

5. FUNDING NUMBERS

C — F19628-90-C-0002
PE — 33142A
PR — 584

6. AUTHOR(S)

Robert J. Figucia

7. PERFORMING ORGANIZATION NAME(S) AND ADDRESS(ES)

Lincoln Laboratory, MIT
P.O. Box 73
Lexington, MA 02173-9108

8. PERFORMING ORGANIZATION REPORT NUMBER

TR-984

9. SPONSORING/MONITORING AGENCY NAME(S) AND ADDRESS(ES)

PM Milstar (Army)
SFAE-CM-MSA
Building 909
Ft. Monmouth, NJ 07703-5508

9

10. SPONSORING/MONITORING AGENCY REPORT NUMBER

ESC-TR-93-236

11. SUPPLEMENTARY NOTES

None

12a. DISTRIBUTION/AVAILABILITY STATEMENT

Approved for public release; distribution is unlimited.

12b. DISTRIBUTION CODE

13. ABSTRACT (*Maximum 200 words*)

The advanced single-channel antijam man portable (ASCAMP) terminal was developed at MIT Lincoln Laboratory as a proof of concept for the Army's SCAMP terminal. The ASCAMP terminal is a 30-lb, extremely high frequency (EHF) satellite communications terminal capable of operating from 75 to 2,400 bps with low inclination, geosynchronous FLTSAT EHF package and Milstar satellites. The terminal was designed to be carried, set up, and operated by a single user. In many instances the control algorithms have been designed to compensate for simplifications made in the hardware to keep the terminal's size, weight, and power to a minimum. This report describes the procedures implemented in the ASCAMP terminal to locate the satellite and synchronize with its downlink. It contains descriptions of the timing and pointing requirements, the procedures for acquisition and tracking, and the measured performance.

14. SUBJECT TERMS

Milstar acquisition
time tracking
angle tracking and
P_r/N_0 estimation
downlink acquisition
spatial tracking
position tracking
SNR estimation
satellite acquisition
satellite tracking
ASCAMP
one-bit demodulation

15. NUMBER OF PAGES
64

16. PRICE CODE

17. SECURITY CLASSIFICATION OF REPORT Unclassified	18. SECURITY CLASSIFICATION OF THIS PAGE Unclassified	19. SECURITY CLASSIFICATION OF ABSTRACT Unclassified	20. LIMITATION OF ABSTRACT Same As Report

NSN 7540-01-280-5500

Standard Form 298 (Rev. 2-89)
Prescribed by AMSI Std. 239-18
298-102